J. Phys. B: At. Mol. Opt. Phys. **40** (2007) 955–974 doi:10.1088/0953-4075/40/5/011

Relativistic many-body calculations of electric-dipole lifetimes, rates and oscillator strengths of $\Delta n = 0$ transitions between $3l^{-1}4l'$ states in Ni-like ions

U I Safronova[1], **A S Safronova**[1] **and P Beiersdorfer**[2]

[1] Physics Department, University of Nevada, Reno, NV 89557, USA
[2] Lawrence Livermore National Laboratory, Livermore, CA 94550, USA

Received 5 January 2007, in final form 21 January 2007
Published 19 February 2007
Online at stacks.iop.org/JPhysB/40/955

Abstract
Transition rates, oscillator strengths and line strengths are calculated for electric-dipole (E1) transitions between odd-parity $3s^23p^63d^94l_1$, $3s^23p^53d^{10}4l_2$ and $3s3p^63d^{10}4l_1$ states and even-parity $3s^23p^63d^94l_2$, $3s^23p^53d^{10}4l_1$ and $3s3p^63d^{10}4l_2$ (with $4l_1 = 4p, 4f$ and $4l_2 = 4s, 4d$) in Ni-like ions with the nuclear charges ranging from $Z = 34$ to 100. Relativistic many-body perturbation theory (RMBPT), including the Breit interaction, is used to evaluate retarded E1 matrix elements in length and velocity forms. The calculations start from a $1s^22s^22p^63s^23p^63d^{10}$ Dirac–Fock potential. First-order RMBPT is used to obtain intermediate coupling coefficients and second-order RMBPT is used to calculate transition matrix elements. Contributions from negative-energy states are included in the second-order E1 matrix elements to ensure the gauge independence of transition amplitudes. Transition energies used in the calculation of oscillator strengths and transition rates are from second-order RMBPT. Lifetimes of the $3s^23p^63d^94d$ levels are given for $Z = 34$–100. These atomic data are important in modelling of M-shell radiation spectra of heavy ions generated in electron beam ion trap experiments and in M-shell diagnostics of plasmas.

(Some figures in this article are in colour only in the electronic version)

1. Introduction

Recently multipole transition wavelengths and rates between the $[3s^23p^63d^94l_1$, $3s^23p^53d^{10}4l_2$ and $3s3p^63d^{10}4l_1]$ excited states and the $3s^23p^63d^{10}$ ground states (3–4 transitions) in nickel-like ions have been calculated using a relativistic many-body theory [1–4]. We continue this work to study atomic characteristics of transitions between the odd-parity $[3s^23p^63d^94l_1$, $3s^23p^53d^{10}4l_2$ and $3s3p^63d^{10}4l_1]$ states and even-parity $[3s^23p^63d^94l_2$, $3s^23p^53d^{10}4l_1$ and $3s3p^63d^{10}4l_2]$ states with $4l_1 = 4p, 4f$ and $4l_2 = 4s, 4d$ (4–4 and 3–3 transitions) in nickel-like ions. The Ni-isoelectronic sequence has been studied extensively in connection with x-ray lasers [5–15]. Recently, an investigation into the use of atomic databases in simulation of Ni-like gadolinium x-ray laser was presented by King *et al* [16]. Several line-overlap measurements relevant to Ni-like x-ray lasers have also been performed [17–19]. In addition, x-ray spectral measurements of the line emission of $n = 3$–4, 3–5, 3–6 and 3–7 transitions in Ni- to Kr-like Au ions in electron beam ion trap (EBIT) plasma were reported by May *et al* [20]. X-ray spectra of Ni-like W including 3–4, 5 and 6 transitions recorded by a broadband microcalorimeter, were analysed in [21, 22]. A detailed analysis of 3–4 and 3–5 transitions in the x-ray spectrum from laser produced plasmas of Ni-like highly charged ions was presented by Doron *et al* [23] (Ba^{28+}), by Zigler *et al* [24] (La^{29+} and Pr^{31+}), by Doron *et al* [25] (Ce^{30+}). Studies of Ni-like ions (Gd^{36+} and W^{46+}) have also been carried out on tokamaks [26, 27]. The spectrum of tungsten is expected to play an important role in tokamak diagnostics with the advent of the International Tokamak Engineering Reactor (ITER), which is expected to use plasma facing components made of tungsten.

Various computer codes were employed to calculate transitions in Ni-like ions. In particular, ab-initio calculations were performed in [23] using the relac relativistic computer code to identify $3d - nf$ ($n = 4$ to 8) transitions of Ni-like Ba. Atomic structure calculations for highly ionized tungsten (Co-like W^{47+} to Rb-like W^{37+}) were done by Fournier [28] with using the graphical angular momentum coupling code ANGULAR and the fully relativistic parametric potential code RELAC. The Hebrew University Lawrence Livermore Atomic Code HULLAC is also based on a relativistic model potential [29]. *Ab initio* calculations with the HULLAC relativistic code was used for detailed analysis of spectral lines by Zigler *et al* [24] and by May *et al* [20]. Zhang *et al* [30], using the Dirac–Fock–Slater (DFS) code evaluated excitation energies and oscillator strengths of 3–4 and 3–5 transitions for the 33 Ni-like ions with $60 \leqslant Z \leqslant 92$. The multiconfiguration Dirac–Fock calculations of the $3d_{3/2}$–$5f_{5/2}$, $3d_{5/2}$–$5f_{7/2}$, $3d_{3/2}$–$6f_{5/2}$, and $3d_{5/2}$–$6f_{7/2}$ transitions were reported by Elliott *et al* [31]. The wavelengths and transition rates for $3l - nl'$ electric-dipole transitions in Ni-like xenon are presented by Skobelev *et al* [32]. Results were obtained by three methods: the relativistic Hartree–Fock (HFR) self-consistent-field method (Cowan code), multiconfiguration Dirac–Fock (MCDH) method (Grant code) and the HULLAC code. The contribution of lots of weak correlation on transition wavelengths and probabilities by including partly single and double excitation from the $3l$ inner-shells into the $4l$ and $5l$ orbital layers of highly charged Ni-like ions were discussed by Dong *et al* [33]. Energy levels, transition probabilities and electron impact excitation for possible x-ray line emissions of Ni-like tantalum ions were recently calculated by Zhong *et al* [34]. Also, the overview of theoretical and experimental works on the $3l - nl'$ transitions in Ni-like ions can be found elsewhere (see, for example, [1–4] and references therein).

There are fewer studies of the 4s–4p and 4p–4d transitions in Ni-like ions [35–42]. Demonstration of soft-x ray amplification in nickel-like ions was reported by MacGowan *et al* [37–39]. The first observation of amplification of spontaneous emission at soft x-ray wavelengths by Eu^{35+} and Yb^{42+} ions was reported in 1987 [37]. The ions were created by high-intensity laser irradiation of a thin foil. Gains of order 1 cm^{-1} were observed on $J = 0$–1, 4d–4p transitions in Eu^{35+}. The Ni-like 4d–4p laser scheme was extended later [38] to wavelengths near the K absorption edge of carbon. Gains of 2.3 cm^{-1} and 2.6 cm^{-1} were observed in Ni-like Ta^{45+} and W^{46+}, respectively. Identification of $n = 4$, $\Delta n = 0$ transitions in the spectra of nickel-like ions from $Z = 37$ (Rb^{9+}) to $Z = 50$ (Sn^{22+}) was reported by Churilov *et al* [36]. The spectra were excited in the laser-produced plasma. Classification of the nickel-like silver and cadmium spectra (Ag^{19+} and Cd^{20+}) from a fast capillary discharge plasma was presented by Rahman *et al* in [40, 41]. Fifty-three Cd XXI and 43 Ag XX transitions ($3d^94p$–$3d^94d$ and $3d^94d$–$3d^94f$) were identified with the assistance of calculations performed using the Slater–Condon method with generalized least-squares fits of the energy parameters

[40, 41]. Recently, the spectrum of nickel-like Kr IX excited in a fast capillary discharge and photographed with high resolution in the 300–800 Å wavelength region was investigated by Churilov *et al* [42]. The analysis was carried out on a basis of the energy parameters interpolation in the Ni I isoelectronic sequence. The 115 spectral lines in Kr^{8+} belonging to the $3d^94s$–$3d^94p$–$3d^94d$–$3d^94f$ transitions were classified for the first time and the complete energy structures of the $3d^94s$, $3d^94p$, $3d^94d$ and $3d^94f$ configurations were presented. The experimental results were confirmed by the generalized least squares (GLS) [42].

A comprehensive survey of M-shell transitions of Au and W produced on the LLNL EBIT was accomplished in [20–22]. Although $\Delta n = 0$ $(n = 4)$ have not yet been observed, such transitions have already been seen in EUV spectra from Rb- to Cu-like Au and W ions [43, 44]. Observation of the 4–4 transitions, however, appear feasible, and future measurements may include these transitions in Ni-like Au and W ions.

In the present paper, relativistic many-body perturbation theory (RMBPT) is used to determine matrix elements, oscillator strengths and transition rates for allowed and forbidden electric-dipole transitions within the $3s^23p^63d^94l$, $3s^23p^53d^{10}4l$ and $3s3p^63d^{10}4l$ complexes of states in Ni-like ions with nuclear charges ranging from $Z = 34$ to 100. Retarded E1 matrix elements are evaluated in both length and velocity forms. These calculations start from a $1s^22s^22p^63s^23p^63d^{10}$ Dirac–Fock potential. First-order perturbation theory is used to obtain intermediate coupling coefficients and second-order RMBPT is used to determine transition matrix elements. Contributions from negative-energy states are included in the second-order $E1$ matrix elements to ensure an agreement between the length-form and velocity-form amplitudes. The transition energies used in the calculation of oscillator strengths and transition rates are obtained from the second-order RMBPT. Lifetimes of the $3s^23p^63d^94d$ levels are given for $Z = 34$–100.

In summary, this work presents both a systematic calculation of the transition probabilities between excited states in Ni-like ions and a study of the importance of the correlation corrections to those properties. The final results are used to calculate lifetimes of levels and to provide benchmark values for Ni-like ions. Our data are compared with the existing measurements.

2. Method

In this section, we write down and discuss the relativistic MBPT formulae for first- and second-order matrix elements for transitions between excited states in atomic systems with one hole in the closed shells and one electron above the closed shells. We consider the coupled states $\Phi_{JM}(a^{-1}v)$ defined by

$$\Phi_{JM}(a^{-1}v) = \sqrt{(2J+1)} \sum_{m_a m_v} (-1)^{j_v - m_v} \begin{pmatrix} j_v & J & j_a \\ -m_v & M & m_a \end{pmatrix} a^{\dagger}_{vm_v} a_{am_a} |0\rangle, \quad (1)$$

where $|0\rangle$ is the closed-shell ground state, the single-particle index v designates the valence state and the single-hole indices a range over the closed core. Below, we use both jj and LS designations for hole–particle states. Instead of using the $a^{-1}v$ designations, we use simpler designations av in all following tables and in the text below.

The first-order reduced electric-dipole matrix element $Z^{(1)}$ for the transition between the hole–particle states $av(J)$–$cw(J')$ is given by

$$Z^{(1)}(av(J), cw(J')) = \sqrt{[J][J']} \left[\delta(c,a) Z(wv) (-1)^{j_v + j_c + 1 + J'} \begin{Bmatrix} J & J' & 1 \\ j_w & j_v & j_a \end{Bmatrix} \right. \\ \left. + \delta(w,v) Z(ac) (-1)^{j_v + j_c + J + 1} \begin{Bmatrix} J & J' & 1 \\ j_c & j_a & j_v \end{Bmatrix} \right], \quad (2)$$

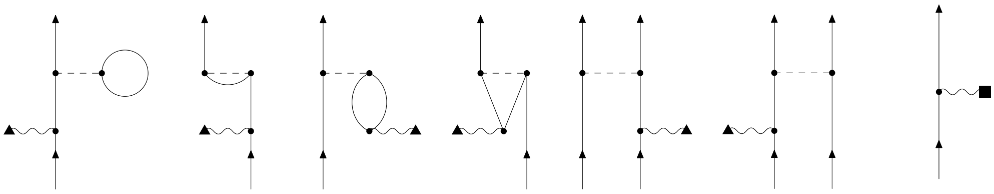

Figure 1. Second-order diagrams for electric-dipole matrix elements.

where $[J] = 2J + 1$. The dipole matrix elements $Z(vw)$, that include retardation, are given in velocity and length forms by equations (3) and (4) of [45].

The second-order reduced matrix element $Z^{(2)}$ for the transition between the hole–particle states $av(J)$–$cw(J')$ consists of four contributions: Dirac–Hartree–Fock (HF) term ($Z^{(\mathrm{HF})}$), random-phase approximation (RPA) term ($Z^{(\mathrm{RPA})}$), correlation contribution (corr) term ($Z^{(\mathrm{corr})}$) and derivative (derv) term, $P^{(\mathrm{derv})}$. The 'HF', 'RPA', 'corr' and 'derv' contributions in second-order matrix elements in terms of Bruckner–Golstone diagrams are illustrated in figure 1. The dashed lines designate Coulomb + Breit interactions and the wavy lines designate interactions with the dipole field. Diagrams 'HF 1' and 'HF 2' as well as diagrams 'RPA 1' and 'RPA 2' are direct and exchange contributions. These diagrams account for the shielding of the dipole field by the core electrons. Diagrams 'corr 1' and 'corr 2' are direct and exchange correlation contributions. These diagrams correct the matrix element to account for interaction between the valence electrons. The 'derv' diagram represents symbolically the second-order RMBPT correction from the derivative term [1]. A detailed discussion of these diagrams for systems with two valence electrons was given by Safronova *et al* [46]. Analytical expressions for the second-order contributions $Z^{(\mathrm{DF})}$, $Z^{(\mathrm{RPA})}$, $Z^{(\mathrm{corr})}$ and $Z^{(\mathrm{derv})}$ for transitions between excited states in hole–particle systems were presented recently [47].

All of the second-order correlation corrections that we discussed above result from the residual Coulomb interaction. To include correlation corrections due to the Breit interaction, the Coulomb matrix element $X_k(abcd)$ must be modified according to the rule

$$X_k(abcd) \to X_k(abcd) + M_k(abcd) + N_k(abcd), \tag{3}$$

where M_k and N_k are magnetic radial integrals defined by equations (A4) and (A5) in [48].

2.1. Uncoupled matrix elements

In table 1, we list values of the first- and second-order contributions to electric-dipole matrix elements $Z^{(\mathrm{DF})}$, $Z^{(\mathrm{RPA})}$, $Z^{(\mathrm{corr})}$, and the matrix element of the derivative term $P^{(\mathrm{derv})}$ for the odd–even $av(J) - a'v'(J')$ transitions with $J = 1$ and $J' = 0$, 1, 2 in Ni-like tungsten, $Z = 74$. Both length and velocity forms of the matrix elements are given. The Coulomb second-order 'HF' contribution $Z^{(\mathrm{HF})}$ vanishes in the present calculation since we use DF basis functions. We use the symbol B in table 1 to denote the Coulomb–Breit contributions to the second-order matrix elements, and we tabulate $B^{(\mathrm{HF})}$, $B^{(\mathrm{RPA})}$, $B^{(\mathrm{corr})}$ and the totals $B^{(2)}$. The first-order contributions $Z^{(\mathrm{DF})}$ are different in length and velocity forms. Also the total second-order Breit corrections $B^{(2)}$ are smaller than the correlation corrections $Z^{(\mathrm{corr})}$ and these correlation contributions are smaller than the RPA terms $Z^{(\mathrm{RPA})}$. The ratios between these terms change with a nuclear charge as illustrated by figure 2 where second-order contributions $Z^{(\mathrm{RPA})}$, $Z^{(\mathrm{corr})}$ and $B^{(2)}$ are shown as functions of Z for the electric-dipole matrix elements

Table 1. Contributions to $E1$ uncoupled reduced matrix elements (au) in length L and velocity V forms for transitions between excited states $av(J)$ and $a'v'(J')$ in W^{46+}.

Coulomb interaction

$av(J)$	$a'v'(J')$		$Z^{(\mathrm{DF})}$	$P^{(\mathrm{derv})}$	$Z^{(\mathrm{RPA})}$	$Z^{(\mathrm{corr})}$
$3p_{1/2}4s_{1/2}(1)$	$3s_{1/2}4s_{1/2}(0)$	(L)	0.109 213	0.109 226	−0.010 600	−0.000 003
		(V)	0.104 743	0.000 032	−0.005 844	−0.003 954
$3s_{1/2}4p_{1/2}(1)$	$3s_{1/2}4s_{1/2}(0)$	(L)	−0.224 466	−0.224 476	0.007 251	0.002 028
		(V)	−0.226 091	−0.000 027	0.008 468	0.011 603
$3d_{5/2}4p_{3/2}(1)$	$3p_{3/2}4p_{3/2}(1)$	(L)	−0.128 829	−0.128 748	0.011 751	−0.001 239
		(V)	−0.123 294	0.000 140	0.005 980	−0.001 724
$3d_{3/2}4p_{3/2}(1)$	$3d_{3/2}4d_{5/2}(1)$	(L)	0.291 004	0.290 928	−0.008 509	−0.003 593
		(V)	0.294 810	−0.000 125	−0.011 747	0.002 303
$3p_{1/2}4s_{1/2}(1)$	$3s_{1/2}4s_{1/2}(1)$	(L)	−0.154 450	−0.154 470	0.014 990	−0.000 954
		(V)	−0.148 130	−0.000 046	0.008 264	−0.001 643
$3p_{3/2}4d_{3/2}(1)$	$3d_{5/2}4d_{3/2}(1)$	(L)	−0.128 829	−0.128 748	0.011 751	0.000 317
		(V)	−0.123 294	0.000 140	0.005 980	0.004 688
$3p_{3/2}4d_{5/2}(1)$	$3d_{5/2}4d_{5/2}(1)$	(L)	−0.160 678	−0.160 577	0.014 656	0.000 472
		(V)	−0.153 774	0.000 174	0.007 458	0.002 461
$3s_{1/2}4p_{3/2}(1)$	$3p_{1/2}4p_{3/2}(1)$	(L)	0.077 225	0.077 235	−0.007 495	−0.000 527
		(V)	0.074 065	0.000 023	−0.004 132	−0.000 029
$3p_{3/2}4d_{3/2}(1)$	$3d_{5/2}4d_{3/2}(2)$	(L)	0.196 790	0.196 666	−0.017 950	−0.000 011
		(V)	0.188 335	−0.000 214	−0.009 135	−0.000 785
$3p_{3/2}4d_{5/2}(1)$	$3d_{5/2}4d_{5/2}(2)$	(L)	0.131 193	0.131 111	−0.011 967	−0.000 670
		(V)	0.125 556	−0.000 142	−0.006 090	−0.003 306
$3p_{3/2}4d_{5/2}(1)$	$3p_{3/2}4p_{3/2}(2)$	(L)	−0.097 001	−0.096 976	0.002 836	0.001 062
		(V)	−0.098 270	0.000 042	0.003 916	−0.001 250
$3s_{1/2}4p_{3/2}(1)$	$3p_{1/2}4p_{3/2}(2)$	(L)	−0.172 681	−0.172 702	0.016 759	−0.001 399
		(V)	−0.165 614	−0.000 051	0.009 239	−0.002 606

Coulomb–Breit interaction

$av(J)$	$a'v'(J')$		$B^{(\mathrm{HF})}$	$B^{(\mathrm{RPA})}$	$B^{(\mathrm{corr})}$	$B^{(2)}$
$3p_{1/2}4s_{1/2}(1)$	$3s_{1/2}4s_{1/2}(0)$	(L)	0.000 187	−0.000 015	0.000 002	0.000 174
		(V)	0.001 605	−0.000 093	−0.000 006	0.001 506
$3s_{1/2}4p_{1/2}(1)$	$3s_{1/2}4s_{1/2}(0)$	(L)	−0.000 289	0.000 010	0.000 008	−0.000 272
		(V)	−0.002 579	−0.000 117	0.000 340	−0.002 356
$3d_{5/2}4p_{3/2}(1)$	$3p_{3/2}4p_{3/2}(1)$	(L)	−0.000 136	0.000 020	−0.000 014	−0.000 130
		(V)	0.000 745	0.000 149	−0.000 004	0.000 890
$3d_{3/2}4p_{3/2}(1)$	$3d_{3/2}4d_{5/2}(1)$	(L)	0.000 228	−0.000 006	0.000 034	0.000 257
		(V)	−0.001 470	0.000 145	0.000 281	−0.001 045
$3p_{1/2}4s_{1/2}(1)$	$3s_{1/2}4s_{1/2}(1)$	(L)	−0.000 265	0.000 022	0.000 000	−0.000 243
		(V)	−0.002 270	0.000 131	0.000 085	−0.002 054
$3p_{3/2}4d_{3/2}(1)$	$3d_{5/2}4d_{3/2}(1)$	(L)	−0.000 136	0.000 020	0.000 006	−0.000 110
		(V)	0.000 745	0.000 149	0.000 044	0.000 939
$3p_{3/2}4d_{5/2}(1)$	$3d_{5/2}4d_{5/2}(1)$	(L)	−0.000 170	0.000 025	−0.000 123	−0.000 267
		(V)	0.000 929	0.000 186	−0.000 221	0.000 894
$3s_{1/2}4p_{3/2}(1)$	$3p_{1/2}4p_{3/2}(1)$	(L)	0.000 133	−0.000 011	0.000 004	0.000 125
		(V)	0.001 135	−0.000 066	−0.000 019	0.001 050
$3p_{3/2}4d_{3/2}(1)$	$3d_{5/2}4d_{3/2}(2)$	(L)	0.000 208	−0.000 031	0.000 005	0.000 182
		(V)	−0.001 138	−0.000 228	−0.000 028	−0.001 394
$3p_{3/2}4d_{5/2}(1)$	$3d_{5/2}4d_{5/2}(2)$	(L)	0.000 139	−0.000 021	0.000 016	0.000 134
		(V)	−0.000 759	−0.000 152	−0.000 071	−0.000 981
$3p_{3/2}4d_{5/2}(1)$	$3p_{3/2}4p_{3/2}(2)$	(L)	−0.000 076	0.000 002	0.000 015	−0.000 059
		(V)	0.000 490	−0.000 048	0.000 056	0.000 498
$3s_{1/2}4p_{3/2}(1)$	$3p_{1/2}4p_{3/2}(2)$	(L)	−0.000 296	0.000 024	−0.000 018	−0.000 290
		(V)	−0.002 538	0.000 147	−0.000 108	−0.002 499

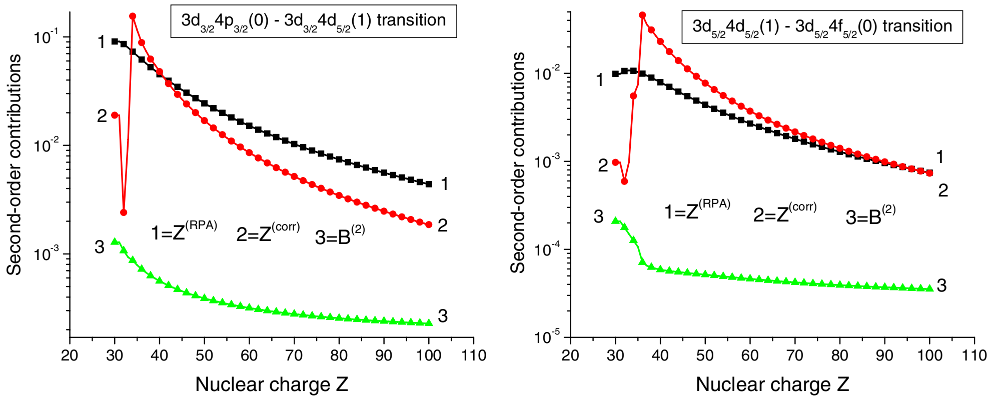

Figure 2. Second-order contributions for electric-dipole matrix elements in Ni-like ions as functions of Z.

$3d_{3/2}4p_{3/2}(0)-3d_{3/2}4d_{5/2}(1)$ and $3d_{5/2}4d_{3/2}(1)-3d_{5/2}4f_{5/2}(0)$. It should be noted that only the $Z^{(\mathrm{corr})}$ terms are non-zero for two-particle transitions such as the $3p_{1/2}4p_{1/2}(1)$–$3p_{3/2}4d_{3/2}(0)$ transition. The values of $Z^{(\mathrm{corr})}$ terms for two-particle transitions are of the same order of magnitude as for the one-particle transitions (for example, $3p_{3/2}4d_{3/2}(1)$–$3d_{3/2}4d_{5/2}(1)$ and $3p_{3/2}4d_{3/2}(1)$–$3d_{3/2}4d_{3/2}(1)$ transitions).

2.2. Coupled matrix elements

As mentioned above, physical hole–particle states are the linear combinations of uncoupled hole–particle states. For the W^{46+} example discussed above, the transition amplitudes between physical states are the linear combinations of the uncoupled transition matrix elements given in table 1. The mixing coefficients and energies are obtained by diagonalizing the first-order effective Hamiltonian which includes both Coulomb and Breit interactions. We let $C_1^{\lambda}(av)$ designate the λth eigenvector of the first-order effective Hamiltonian and let E_1^{λ} be the corresponding eigenvalue. The coupled transition matrix element between the initial eigenstate I with the angular momentum J and the final state F with the angular momentum J' is given by

$$\begin{aligned}Q^{(1+2)}(\mathrm{I}-\mathrm{F}) = {} & \frac{1}{E_1^{\mathrm{I}}-E_1^{\mathrm{F}}}\sum_{av}\sum_{cw} C_1^{\mathrm{I}}(av)C_1^{\mathrm{F}}(cw) \\ & \times \left\{[\varepsilon_{av}-\varepsilon_{cw}]\left[Z_1^{(1+2)}[av(J)-cw(J')]+B_1^{(2)}[av(J)-cw(J')]\right]\right. \\ & \left.+\left[E_1^{\mathrm{I}}-E_1^{\mathrm{F}}-\varepsilon_{av}+\varepsilon_{cw}\right]\mathrm{P}_1^{(\mathrm{derv})}[av(J)-cw(J')]\right\}. \end{aligned} \quad (4)$$

Here, $\varepsilon_{av}=-\varepsilon_a+\varepsilon_v$ and $Z_1^{(1+2)}=Z^{(\mathrm{DF})}+Z^{(\mathrm{RPA})}+Z^{(\mathrm{corr})}$, and $B_1^{(2)}=B^{(\mathrm{HF})}+B^{(\mathrm{RPA})}+B^{(\mathrm{corr})}$. Using these formulae together with the uncoupled reduced matrix elements given in table 1, we transform the uncoupled matrix elements to matrix elements between coupled (physical) states.

Values of *coupled* reduced matrix elements in length and velocity forms are given in table 2 for the transitions considered in table 1. Although we use an intermediate-coupling scheme, it is nevertheless convenient to label the physical states using the LS scheme. Both designations are given in table 2. We see that L and V forms of the coupled matrix elements in table 2 differ only in the third or fourth digits. These L–V differences arise because we start

Table 2. Coupled reduced matrix elements Q calculated in length L and velocity V forms for W^{46+}.

		First order		RMBPT			
$l_1l_2\ LSJ$	$l_3l_4\ L'S'J'$	L	V	L	V	$j_1j_2\ (J)$	$j_3j_4\ (J')$
3p4s $^3P_1$	3s4s $^1S_0$	0.105 99	0.101 59	0.096 05	0.096 07	$3p_{1/2}4s_{1/2}(1)$	$3s_{1/2}4s_{1/2}(0)$
3s4p $^3P_1$	3s4s $^1S_0$	0.107 49	0.108 30	0.102 30	0.102 29	$3s_{1/2}4p_{1/2}(1)$	$3s_{1/2}4s_{1/2}(0)$
3d4p $^3D_1$	3p4p $^3S_1$	0.129 01	0.123 70	0.118 66	0.118 59	$3d_{5/2}4p_{3/2}(1)$	$3p_{3/2}4p_{3/2}(1)$
3d4p $^1P_1$	3d4d $^3P_1$	0.281 77	0.285 58	0.271 97	0.271 92	$3d_{3/2}4p_{3/2}(1)$	$3d_{3/2}4d_{5/2}(1)$
3d4f $^3D_1$	3d4d $^3S_1$	0.305 33	0.314 64	0.290 29	0.290 27	$3d_{5/2}4f_{7/2}(1)$	$3d_{5/2}4d_{3/2}(1)$
3p4s $^3P_1$	3s4s $^3S_1$	0.203 89	0.197 56	0.188 71	0.188 67	$3p_{1/2}4s_{1/2}(1)$	$3s_{1/2}4s_{1/2}(1)$
3p4d $^3P_1$	3d4d $^3S_1$	0.112 25	0.106 96	0.100 64	0.100 58	$3p_{3/2}4d_{3/2}(1)$	$3d_{5/2}4d_{3/2}(1)$
3p4d $^1P_1$	3d4d $^1P_1$	0.151 40	0.144 68	0.137 87	0.137 75	$3p_{3/2}4d_{5/2}(1)$	$3d_{5/2}4d_{5/2}(1)$
3s4p $^1P_1$	3p4p $^3P_1$	0.132 36	0.128 87	0.122 00	0.122 06	$3s_{1/2}4p_{3/2}(1)$	$3p_{1/2}4p_{3/2}(1)$
3d4f $^3P_1$	3d4s $^1D_2$	0.032 99	0.031 36	0.029 99	0.030 00	$3d_{5/2}4f_{5/2}(1)$	$3d_{3/2}4s_{1/2}(2)$
3d4f $^1P_1$	3p4f $^3D_2$	0.065 62	0.062 43	0.054 45	0.054 42	$3d_{3/2}4f_{5/2}(1)$	$3p_{3/2}4f_{5/2}(2)$
3p4s $^3P_1$	3s4d $^1D_2$	0.012 02	0.011 47	0.012 09	0.012 09	$3p_{1/2}4s_{1/2}(1)$	$3s_{1/2}4d_{5/2}(2)$
3p4d $^3P_1$	3d4d $^3P_2$	0.192 27	0.184 04	0.174 36	0.174 26	$3p_{3/2}4d_{3/2}(1)$	$3d_{5/2}4d_{3/2}(2)$
3p4d $^3P_1$	3d4d $^1D_2$	0.058 44	0.055 74	0.053 24	0.053 21	$3p_{3/2}4d_{3/2}(1)$	$3d_{3/2}4d_{3/2}(2)$
3p4d $^1P_1$	3d4d $^3P_2$	0.012 93	0.012 31	0.012 20	0.012 20	$3p_{3/2}4d_{5/2}(1)$	$3d_{5/2}4d_{3/2}(2)$
3p4d $^1P_1$	3d4d $^3D_2$	0.127 87	0.122 31	0.115 79	0.115 77	$3p_{3/2}4d_{5/2}(1)$	$3d_{5/2}4d_{5/2}(2)$
3p4d $^1P_1$	3d4d $^1D_2$	0.070 50	0.067 18	0.064 56	0.064 57	$3p_{3/2}4d_{5/2}(1)$	$3d_{3/2}4d_{5/2}(2)$
3p4d $^1P_1$	3p4p $^1D_2$	0.076 34	0.077 50	0.073 56	0.073 60	$3p_{3/2}4d_{5/2}(1)$	$3p_{3/2}4p_{3/2}(2)$
3s4p $^3P_1$	3s4d $^1D_2$	0.011 13	0.010 92	0.010 22	0.010 22	$3s_{1/2}4p_{1/2}(1)$	$3s_{1/2}4d_{5/2}(2)$
3s4p $^1P_1$	3p4p $^3P_2$	0.170 15	0.163 04	0.156 15	0.156 06	$3s_{1/2}4p_{3/2}(1)$	$3p_{1/2}4p_{3/2}(2)$

our RMBPT calculations using a non-local Dirac–Fock (DF) potential. If we were to replace the DF potential by a local potential, the differences would disappear completely. The first two columns in table 2 show L and V values of *coupled* reduced matrix elements calculated without the second-order contribution. As we see from this table, removing the second-order contribution increases the $L - V$ differences.

It should be emphasized that we include negative energy state (NES) contributions into the sums over the intermediate states. Ignoring the NES contributions leads only to small changes in the L-form matrix elements but to substantial changes in some of the V-form matrix elements, with a consequent loss of gauge independence for a local potential.

2.3. Negative-energy contributions

The NES contributions to the second-order reduced matrix elements arise from the terms in the sums over states i and n in the $Z^{(\mathrm{corr})}$ contributions [47] for which $\varepsilon_i < -mc^2$. The NES contributions for non-relativistically allowed transitions were discussed in [3] for Ni-like ions, where they were found to be the most important for velocity-form matrix elements; they do not significantly modify length-form matrix elements. In [45], it was shown that NES contributions can be of the same order of magnitude as the 'regular' positive-energy contributions for certain non-relativistically forbidden transitions in Be-like ions. We observe similar large contributions here for LS-forbidden transitions. The matrix elements in tables 1 and 2 include NES contributions.

In figure 3, we illustrate the Z-dependence of the differences between line strengths calculated in length S_L and velocity S_V forms for the 3d4d $^3G_5$–3d4f $^3H_6$ and

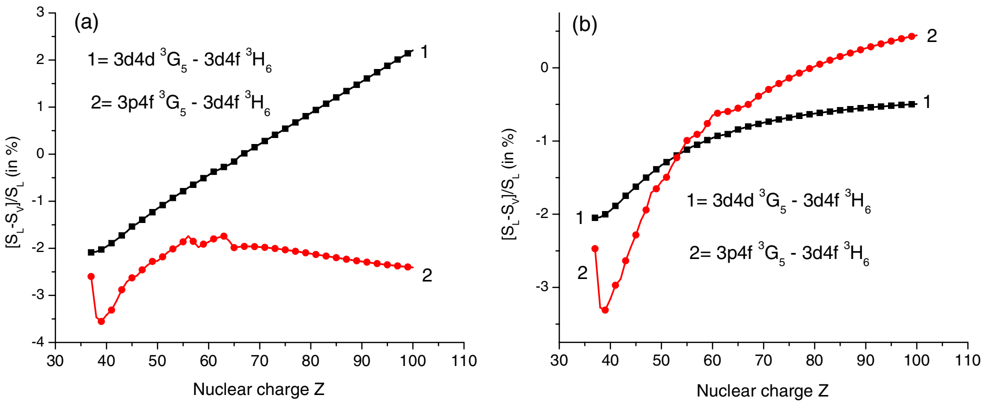

Figure 3. Difference between the values of line strengths calculated in length (S_L) and velocity (S_V) gauges for E1 transitions in Ni-like ions as functions of Z. Graph (a) shows data without NES contributions and graph (b) shows data with NES contributions.

3p4f ^{3}G$_5$–3d4f ^{3}H$_6$ transitions. We plot the ratio $(S_L - S_V)/S_L$ (in percent) calculated without (a) and with (b) negative-energy state contributions to the second-order reduced matrix elements. The ratio $(S_L - S_V)/S_L$ for the 3d4d ^{3}G$_5$–3d4f ^{3}H$_6$ transition decreases from 2% to 1% for $Z = 34$ up to $Z = 100$. The ratio $(S_L - S_V)/S_L$ decreases substantially (from 3% to 0% for high Z) when NES are included for the 3p4f ^{3}G$_5$–3d4f ^{3}H$_6$ transition.

In view of the gauge dependence issue discussed above, our results below are presented in L form to decrease the volume of tabulated material. Uncertainties in the recommended values given in [49] were estimated to be less than 10% based on comparisons with experimental results from lifetime and emission measurements. The agreement between theoretical L-form and V-form results was also used in [49] as an indicator of accuracy. Since the present transition data are obtained using a single method for all Z, and improve in accuracy with increasing Z, we expect our data for high Z to be very reliable.

3. Results and discussion

We calculate line strengths, oscillator strengths and transition probabilities for 1549 $[3l_1 4l_2\ ^{1,3}L_J - 3l_3 4l_4\ ^{1,3}L'_{J'}]$ lines for all ions with $Z = 32$–100. The results were calculated in both length and velocity forms but, since the L form is less sensitive to various contributions, only length-form results are presented in the following tables and figures. The theoretical energies used to evaluate oscillator strengths and transition probabilities are calculated using the second-order RMBPT formalism developed in [1].

3.1. Transition rates

The general trends of the Z-dependence of transition rates for the $3l_1 4l_2\ ^{1,3}L_J$–$3l_3 4l_4\ ^{1,3}L'_{J'}$ lines are presented in figures 4 and 5. Each part in figure 4 shows transitions to a fixed J state from states belonging to a limited set of states $3l4l'\ ^{1,3}L_J$, i.e. a *complex* of states. A complex includes all states of the same parity and J obtained from the combinations of the $3l4l'\ ^{1,3}L_J$ states. For example, the odd-parity complex with $J = 1$ includes the states 3s4p ^{1,3}P$_1$, 3p4s ^{1,3}P$_1$, 3p4d ^{3}D$_1$, 3p4d ^{1,3}P$_1$, 3d4p ^{3}D$_1$, 3d4p ^{1,3}P$_1$, 3d4f ^{3}D$_1$ and 3d4f ^{1,3}P$_1$ in LS coupling or 3s4p$_{1/2}$(1), 3s4p$_{3/2}$(1), 3p$_{1/2}$4s(1), 3p$_{3/2}$4s(1), 3p$_{1/2}$4d$_{3/2}$(1), 3p$_{3/2}$4d$_{3/2}$(1),

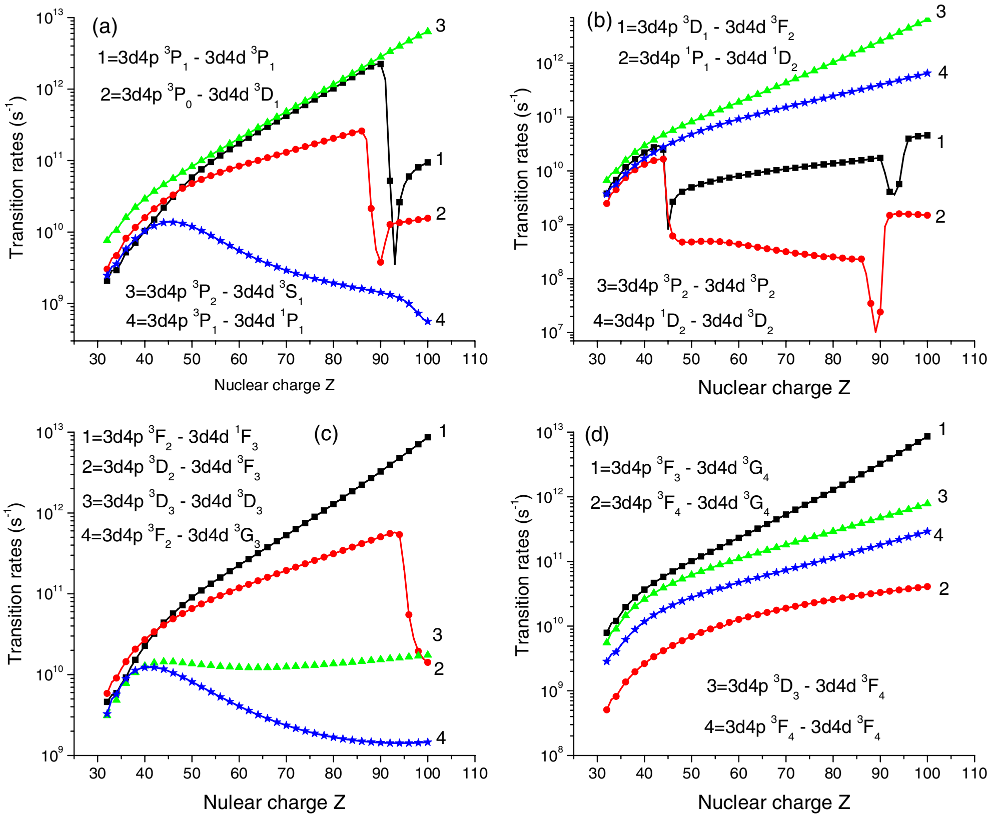

Figure 4. Transition rates for odd–even transitions in Ni-like ions as function of Z.

$3p_{3/2}4d_{5/2}(1)$, $3d_{3/2}4p_{1/2}(1)$, $3d_{3/2}4p_{3/2}(1)$, $3d_{5/2}4p_{3/2}(1)$, $3d_{3/2}4f_{5/2}(1)$, $3d_{5/2}4f_{5/2}(1)$ and $3d_{5/2}4f_{7/2}(1)$ in jj coupling. Later, we use the LS designations since they are more conventional.

In figures 4(a)–(d), we present a limited set (16 among 123) of transition probabilities for the 3d4p–3d4d lines. The 3d4p–3d4d transitions are illustrated by 3d4p $^{1,3}\mathrm{P}_J$–3d4d $^{1,3}L_1$, 3d4p $^{1,3}L'_J$ − 3d4d $^{1,3}L_2$, 3d4p $^{1,3}L'_J$ − 3d4d $^{1,3}L_3$, 3d4p $^{3}L'_J$ − 3d4d $^{3}L_4$ transitions shown in figures 4(a)–(d), respectively.

In figures 5(a) and (b), we present a limited set (8 among 36) of transition rates for the 3d4s–3d4p lines. The eight 3d4d–3d4f transitions (among 171 transitions) are presented in figures 5(c) and (d). Transition rates for the two 3d4s $^{1,3}\mathrm{D}_{J'}$ − 3d4f $^{1,3}L_J$ lines (among 42 lines) are shown in figure 5(c). It should be noted that all transitions shown in figures 4 and 5 are the allowed one-particle (4p − 4d transitions in figure 4 and 4s − 4p, 4d − 4f transitions in figure 5), except two transitions shown in figure 5(c). The latter ones are the 4s–4f transitions to be forbidden as dipole-electric one-particle transitions. The value of transition rates for these transitions are not zero because of two-particle interactions; between the [3d4s + 3d4d + 3s4s] and [3d4f + 3d4p + 3s4f] configurations as well as because of the second-order contribution from correlation diagrams ($Z^{\mathrm{corr}}(3d_{5/2}4s_{1/2}(2) - 3d_{5/2}4f_{5/2}(1)) = 0.842\,874 \times 10^{-4}$ and $Z^{\mathrm{corr}}(3d_{3/2}4s_{1/2}(2)$–$3d_{5/2}4f_{5/2}(1)) = -0.131\,785 \times 10^{-3}$). We can see from figure 5(c), that the transition rates of these two-particle 3d4s $^{1,3}\mathrm{D}_{J'}$–3d4f $^{1,3}L_J$ lines are smaller (by 2–4 orders

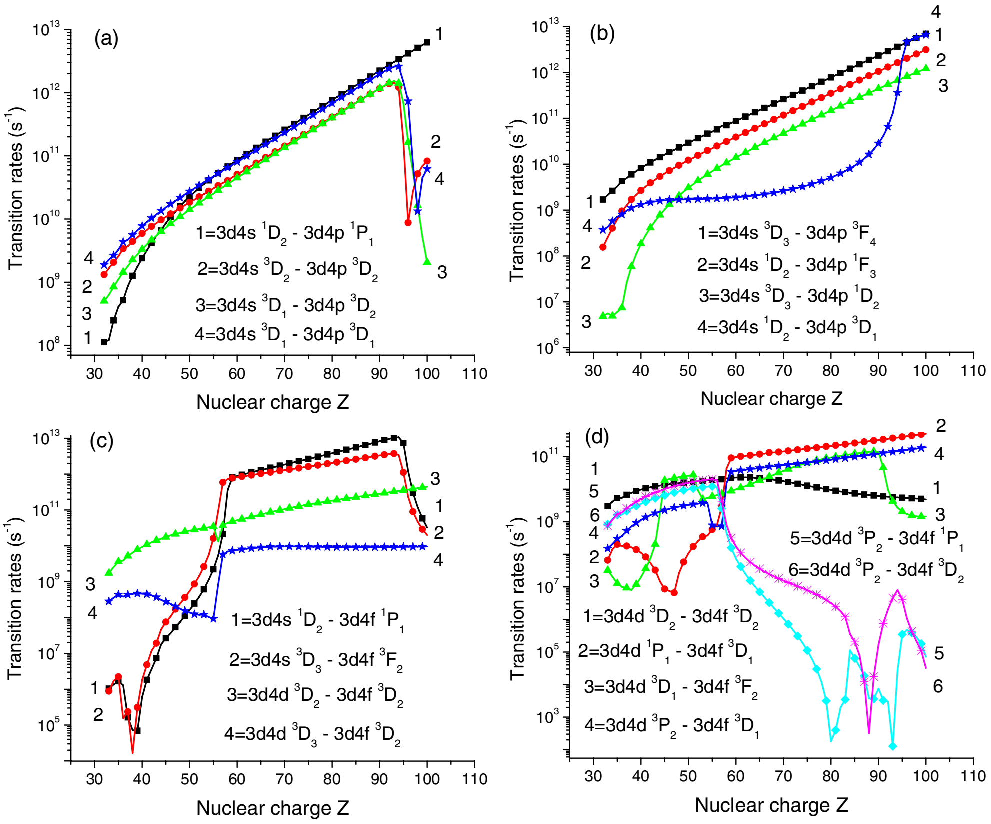

Figure 5. Transition rates for even–odd transitions in Ni-like ions as function of Z.

of magnitude) than the transition rates of one-particle 3d4d $^3D_{J'}$–3d4f ^3D_J lines for small Z but become even larger for high Z.

We see from the graphs that transitions with smooth Z dependences are rarer than transitions with sharp features but still occur for all transition types: triplet–triplet, singlet–singlet, and singlet–triplet, and include transitions with both small J and large J. One general conclusion that can be derived from those graphs is that the smooth Z-dependences occur more frequently for transitions with the largest values of transition rates among the transitions inside complexes.

Singularities in the transition-rate curves have three distinct origins: avoided level crossings, zeros in the dipole matrix elements and zeros in transition energies. Avoided level crossings result in changes of the dominant level configuration at a particular value of Z and lead to abrupt changes in the transition rate curves when the partial rates associated with the dominant configurations below and above the crossing point are significantly different. Zeros in transition matrix elements as functions of Z lead to cusp-like minima in the transition rate curves. Zeros in transition energies, occurring at high Z listed in table 3, also result in cusp-like minima in the transition rate curves. Examples of each of these three singularity types can be seen in figures 4 and 5. Dramatic examples of the first type, avoided level crossings, are seen in figure 4(a) at $Z = 90$, corresponding to a change in the dominant configuration for the 3d4d $^3D_1$ state, the $3p_{3/2}4p_{1/2}(1)$ instead of the $3d_{3/2}4d_{3/2}(1)$ configuration. An avoided level crossing also occurs for the 3d4p $^3P_1$–3d4d $^3P_1$ transition figure 4(a) at $Z = 93$. Examples

Table 3. Level inversions in Ni-like ions. Level inversions occur at the interface between the upper even- and odd-parity groups at high Z where the 13 even-parity levels 3d4d LSJ cross various levels of the upper odd-parity group (3d4f LSJ and 3d4p LSJ) as Z increases. We list in the values of Z for which each of these even-parity levels crosses a given level of the odd-parity group.

	3d4d					3d4d				3d4d			
Levels	^{3}P$_1$	^{3}D$_1$	^{1}P$_1$	^{3}S$_1$	^{1}D$_2$	^{3}F$_2$	^{3}D$_2$	^{3}P$_2$	^{1}F$_3$	^{3}F$_3$	^{3}D$_3$	^{3}F$_4$	^{3}G$_4$
3d4f ^{3}P$_2$	77	80	89		76	79	88		76	80	88		
3d4f ^{3}D$_2$									95				
3d4f ^{1}D$_2$									99				
3d4f ^{3}D$_3$									96			97	
3d4f ^{3}G$_3$									100				
3d4f ^{3}H$_4$									96			97	
3d4f ^{3}G$_4$									99				
3d4f ^{3}H$_5$												96	
3d4f ^{3}G$_5$												100	
3d4p ^{3}P$_0$				95									
3d4p ^{3}D$_2$				94									
3d4p ^{3}D$_3$								95					95

of the second type, zeros in matrix elements, are seen in figure 5(d) at $Z = 45$–46 for the 3d4d ^{1}P$_1$–3d4f ^{3}D$_1$ transition and at $Z = 55$–56 for the 3d4d ^{3}D$_1$–3d4f ^{3}F$_2$ transition. Finally, singularities of the third type, corresponding to an energy of almost zero are seen at $Z = 88$ for the transition in 3d4d ^{3}P$_2$–3d4f ^{3}D$_2$ in figure 5(d) and at $Z = 80$ and 93 for the 3d4d ^{3}P$_2$–3d4f ^{1}P$_1$ transition in figure 5(d). For both cases the inversion of levels involved in transitions occurs as demonstrated in table 3 (3d4d ^{3}P$_2$, 3d4f ^{3}D$_2$ levels and 3d4d ^{3}P$_2$, 3d4f ^{1}P$_1$ levels).

3.2. Wavelengths and transition rates

In table 4, wavelengths and electric-dipole transition rates for 3d4p–3d4d transitions in Ni-like Kr are presented. We limit the table to the transitions given in [42]. To avoid level identification problems, we present the LS and jj labels of the transitions and include both wavelengths and transition rates in tables 4. We note that only the transitions with the largest values of A were experimentally observed. It should be noted that we arrange the data in groups with a fixed LSJ level of the upper state. We see from the comparison of RMBPT and experimental data in table 4, that the agreement in wavelengths is about 0.1–0.5%. It should be noted that the accuracy of the second-order RMBPT method increases with increasing a nuclear charge.

Transition rates in [42] were calculated in the Racah–Slater formalism by means of the RCN, RCG Cowan computer codes [50], using scaled Hartree–Fock (HF) integrals as initial parameters. The sets of the even $3d^{10}$, $3d^9ns$ ($n = 4$–6), $3d^9nd$ ($n = 4$–6), $3d^84s^2$, $3d^84s4d$, $3p^53d^{10}4p$ and $3p^53d^{10}4f$ configurations and the odd $3d^9np$ ($n = 4$–6), $3d^9nf$ ($n = 4$–6), $3d^84s4p$, $3d^84s4f$ and $3p^53d^{10}4s$, $3p^53d^{10}4d$ configurations have been used in these calculations. Highly excited configurations have been included as they have large integrals of interaction with the analysed $3d^9\,4l$ configurations [42]. The second-order RMBPT calculation includes partial waves up to $l_{\rm max} = 8$ and is extrapolated to account for contributions from higher partial waves. We use B-spline methods [51] to generate a complete set of basis DF wavefunctions for use in the evaluation of RMBPT expressions. For Ni-like ions, we use 50 splines of order $k = 8$ for each angular momentum. In table 4, the RMBPT transition rates (gA_r) are compared with results given by Churilov *et al* [42]. The difference

Table 4. Wavelengths (λ in Å) and transition rates (gA in 10^9 s^{-1}) for 3d4p–3d4d transitions in Ni-like krypton, $Z = 36$. The RMBPT results are compared with experimental wavelengths results and COWAN data presented by Churilov *et al* [42].

Transitions, jj-coupling		λ (Å)		gA (10^9 s^{-1})		Transitions, LS-coupling	
Lower	Upper	RMBPT	Expt.	RMBPT	COWAN	Lower	Upper
$3d_{5/2}4p_{3/2}$ (1)	$3d_{3/2}4d_{3/2}$ (0)	345.000	328.640	29.1	34.9	3d4p $^1P_1$	3d4d $^1S_0$
$3d_{3/2}4p_{1/2}$ (1)	$3d_{5/2}4d_{5/2}$ (0)	401.367	401.993	22.8	23.8	3d4p $^3P_1$	3d4d $^3P_0$
$3d_{3/2}4p_{3/2}$ (1)	$3d_{5/2}4d_{5/2}$ (0)	437.084	437.935	0.9	0.9	3d4p $^3D_1$	3d4d $^3P_0$
$3d_{3/2}4p_{1/2}$ (1)	$3d_{3/2}4d_{3/2}$ (1)	399.558	398.826	15.6	14.2	3d4p $^3P_1$	3d4d $^3P_1$
$3d_{3/2}4p_{3/2}$ (0)	$3d_{3/2}4d_{3/2}$ (1)	411.080	409.612	11.5	11.1	3d4p $^3P_0$	3d4d $^3P_1$
$3d_{5/2}4p_{3/2}$ (1)	$3d_{3/2}4d_{3/2}$ (1)	423.113	423.260	11.0	10.6	3d4p $^1P_1$	3d4d $^3P_1$
$3d_{3/2}4p_{3/2}$ (1)	$3d_{3/2}4d_{3/2}$ (1)	434.939	434.170	12.8	14.1	3d4p $^3D_1$	3d4d $^3P_1$
$3d_{3/2}4p_{3/2}$ (2)	$3d_{3/2}4d_{3/2}$ (1)	438.181	437.838	11.8	11.0	3d4p $^3D_2$	3d4d $^3P_1$
$3d_{3/2}4p_{1/2}$ (1)	$3d_{3/2}4d_{5/2}$ (1)	393.254	392.537	6.0	8.3	3d4p $^3P_1$	3d4d $^3D_1$
$3d_{5/2}4p_{3/2}$ (2)	$3d_{3/2}4d_{5/2}$ (1)	396.486	396.295	6.4	5.6	3d4p $^3F_2$	3d4d $^3D_1$
$3d_{3/2}4p_{3/2}$ (0)	$3d_{3/2}4d_{5/2}$ (1)	404.411	402.961	24.5	25.7	3d4p $^3P_0$	3d4d $^3D_1$
$3d_{5/2}4p_{3/2}$ (1)	$3d_{3/2}4d_{5/2}$ (1)	416.050	416.159	17.3	19.6	3d4p $^1P_1$	3d4d $^3D_1$
$3d_{3/2}4p_{3/2}$ (1)	$3d_{3/2}4d_{5/2}$ (1)	427.480	426.708	13.9	11.0	3d4p $^3D_1$	3d4d $^3D_1$
$3d_{5/2}4p_{1/2}$ (2)	$3d_{5/2}4d_{3/2}$ (1)	408.261	413.728	47.9	50.3	3d4p $^3P_2$	3d4d $^3S_1$
$3d_{3/2}4p_{1/2}$ (1)	$3d_{5/2}4d_{3/2}$ (1)	427.610	433.066	10.5	12.0	3d4p $^3P_1$	3d4d $^3S_1$
$3d_{5/2}4p_{1/2}$ (2)	$3d_{5/2}4d_{5/2}$ (1)	393.451	393.244	12.8	16.1	3d4p $^3P_2$	3d4d $^1P_1$
$3d_{3/2}4p_{1/2}$ (1)	$3d_{5/2}4d_{5/2}$ (1)	411.391	410.676	17.3	18.5	3d4p $^3P_1$	3d4d $^1P_1$
$3d_{3/2}4p_{1/2}$ (2)	$3d_{5/2}4d_{5/2}$ (1)	430.632	429.881	9.7	10.3	3d4p $^1D_2$	3d4d $^1P_1$
$3d_{5/2}4p_{3/2}$ (1)	$3d_{5/2}4d_{5/2}$ (1)	436.406	436.640	14.1	14.7	3d4p $^1P_1$	3d4d $^1P_1$
$3d_{5/2}4p_{3/2}$ (2)	$3d_{3/2}4d_{3/2}$ (2)	390.845	389.737	6.2	8.7	3d4p $^3F_2$	3d4d $^3F_2$
$3d_{3/2}4p_{3/2}$ (1)	$3d_{3/2}4d_{3/2}$ (2)	420.930	419.130	58.3	66.1	3d4p $^3D_1$	3d4d $^3F_2$
$3d_{3/2}4p_{3/2}$ (2)	$3d_{3/2}4d_{3/2}$ (2)	423.966	422.533	33.2	29.3	3d4p $^3D_2$	3d4d $^3F_2$
$3d_{5/2}4p_{3/2}$ (2)	$3d_{3/2}4d_{5/2}$ (2)	387.285	386.632	32.4	33.3	3d4p $^3F_2$	3d4d $^1D_2$
$3d_{3/2}4p_{1/2}$ (2)	$3d_{3/2}4d_{5/2}$ (2)	400.931	399.709	10.9	11.7	3d4p $^1D_2$	3d4d $^1D_2$
$3d_{5/2}4p_{3/2}$ (1)	$3d_{3/2}4d_{5/2}$ (2)	405.931	405.530	37.4	45.0	3d4p $^1P_1$	3d4d $^1D_2$
$3d_{3/2}4p_{3/2}$ (1)	$3d_{3/2}4d_{5/2}$ (2)	416.804	415.530	9.4	6.9	3d4p $^3D_1$	3d4d $^1D_2$
$3d_{3/2}4p_{3/2}$ (2)	$3d_{3/2}4d_{5/2}$ (2)	419.780	418.899	16.6	19.9	3d4p $^3D_2$	3d4d $^1D_2$
$3d_{5/2}4p_{1/2}$ (2)	$3d_{5/2}4d_{3/2}$ (2)	390.896	393.075	78.6	86.9	3d4p $^3P_2$	3d4d $^3P_2$
$3d_{5/2}4p_{1/2}$ (3)	$3d_{5/2}4d_{3/2}$ (2)	400.252	401.899	8.2	9.3	3d4p $^3F_3$	3d4d $^3F_2$
$3d_{5/2}4p_{3/2}$ (3)	$3d_{5/2}4d_{3/2}$ (2)	430.089	432.351	20.4	21.5	3d4p $^3D_3$	3d4d $^3P_2$
$3d_{3/2}4p_{1/2}$ (1)	$3d_{5/2}4d_{5/2}$ (2)	401.380	400.529	31.3	36.1	3d4p $^3P_1$	3d4d $^3D_2$
$3d_{5/2}4p_{3/2}$ (2)	$3d_{5/2}4d_{5/2}$ (2)	404.749		11.4		3d4p $^3F_2$	3d4d $^3D_2$
$3d_{3/2}4p_{1/2}$ (2)	$3d_{5/2}4d_{5/2}$ (2)	419.676	418.783	44.1	48.1	3d4p $^1D_2$	3d4d $^3D_2$
$3d_{3/2}4p_{3/2}$ (2)	$3d_{5/2}4d_{5/2}$ (2)	440.374	439.900	4.6	6.2	3d4p $^3D_2$	3d4d $^3D_2$
$3d_{5/2}4p_{1/2}$ (3)	$3d_{3/2}4d_{3/2}$ (3)	386.978	385.676	8.0	18.2	3d4p $^3F_3$	3d4d $^1F_3$
$3d_{5/2}4p_{3/2}$ (2)	$3d_{3/2}4d_{3/2}$ (3)	398.033	397.394	64.4	56.0	3d4p $^3F_2$	3d4d $^1F_3$
$3d_{3/2}4p_{1/2}$ (2)	$3d_{3/2}4d_{3/2}$ (3)	412.460	411.217	61.4	86.5	3d4p $^1D_2$	3d4d $^1F_3$
$3d_{3/2}4p_{3/2}$ (3)	$3d_{3/2}4d_{3/2}$ (3)	422.300	423.915	7.2	8.7	3d4p $^3D_3$	3d4d $^3G_3$
$3d_{3/2}4p_{3/2}$ (2)	$3d_{3/2}4d_{3/2}$ (3)	432.436	431.547	3.3	3.3	3d4p $^1D_2$	3d4d $^1F_3$
$3d_{3/2}4p_{3/2}$ (3)	$3d_{3/2}4d_{5/2}$ (3)	410.566	409.432	35.4	33.3	3d4p $^3F_3$	3d4d $^1F_3$
$3d_{3/2}4p_{3/2}$ (2)	$3d_{3/2}4d_{5/2}$ (3)	420.140	418.926	101.2	114.1	3d4p $^3D_2$	3d4d $^3F_3$
$3d_{5/2}4p_{1/2}$ (2)	$3d_{5/2}4d_{3/2}$ (3)	388.512	388.717	47.4	52.9	3d4p $^3P_2$	3d4d $^3D_3$
$3d_{5/2}4p_{1/2}$ (3)	$3d_{5/2}4d_{3/2}$ (3)	397.752	397.329	25.2	28.2	3d4p $^3F_3$	3d4d $^3D_3$
$3d_{5/2}4p_{3/2}$ (4)	$3d_{5/2}4d_{3/2}$ (3)	411.061		11.8		3d4p $^3F_4$	3d4d $^3D_3$
$3d_{5/2}4p_{3/2}$ (3)	$3d_{5/2}4d_{3/2}$ (3)	427.204	427.064	54.5	56.8	3d4p $^3D_3$	3d4d $^3D_3$
$3d_{3/2}4p_{3/2}$ (3)	$3d_{5/2}4d_{3/2}$ (3)	435.163	435.437	10.3	13.9	3d4p $^1F_3$	3d4d $^3D_3$
$3d_{5/2}4p_{1/2}$ (3)	$3d_{5/2}4d_{5/2}$ (3)	395.445	394.596	35.0	31.0	3d4p $^3F_3$	3d4d $^3G_3$

Table 4. (Continued.)

Transitions, jj-coupling		λ (Å)		gA (10^9 s^{-1})		Transitions, LS-coupling	
Lower	Upper	RMBPT	Expt.	RMBPT	COWAN	Lower	Upper
$3d_{5/2}4p_{3/2}$ (2)	$3d_{5/2}4d_{5/2}$ (3)	406.997	406.864	62.0	94.8	3d4p $^3F_2$	3d4d $^3G_3$
$3d_{3/2}4p_{1/2}$ (2)	$3d_{5/2}4d_{5/2}$ (3)	422.094	421.368	40.2	28.8	3d4p $^1D_2$	3d4d $^3G_3$
$3d_{3/2}4p_{3/2}$ (2)	$3d_{5/2}4d_{5/2}$ (3)	443.037	442.752	0.8	1.6	3d4p $^1D_2$	3d4d $^3G_3$
$3d_{3/2}4p_{3/2}$ (3)	$3d_{3/2}4d_{5/2}$ (4)	418.412	417.594	168.3	194.5	3d4p $^1F_3$	3d4d $^1G_4$
$3d_{5/2}4p_{1/2}$ (3)	$3d_{5/2}4d_{3/2}$ (4)	403.991	403.214	177.8	205.3	3d4p $^3F_3$	3d4d $^3G_4$
$3d_{5/2}4p_{3/2}$ (4)	$3d_{5/2}4d_{3/2}$ (4)	417.728		12.3		3d4p $^3F_4$	3d4d $^3G_4$
$3d_{5/2}4p_{3/2}$ (3)	$3d_{5/2}4d_{3/2}$ (4)	434.409	433.885	6.4	7.1	3d4p $^3D_3$	3d4d $^3G_4$
$3d_{5/2}4p_{3/2}$ (4)	$3d_{5/2}4d_{5/2}$ (4)	405.163	404.403	55.7	54.6	3d4p $^3F_4$	3d4d $^3F_4$
$3d_{5/2}4p_{3/2}$ (3)	$3d_{5/2}4d_{5/2}$ (4)	420.837	420.398	131.5	153.1	3d4p $^3D_3$	3d4d $^3F_4$
$3d_{5/2}4p_{3/2}$ (4)	$3d_{5/2}4d_{5/2}$ (5)	417.814	416.756	224.2	255.1	3d4p $^3F_4$	3d4d $^3G_5$

Table 5. Wavelengths (λ in Å) and transition rates (gA in 10^9 s^{-1}) for 3d4s–3d4p transitions in Ni-like Pd^{18+} and Cd^{20+}. The RMBPT results are compared with experimental measurements of wavelengths and intensities in relative units by Churilov *et al* [36].

Transitions 3d4s	3d4p	RMBPT λ (Å)	Experimental λ (Å)	RMBPT gA	Experimental intensities	RMBPT λ (Å)	Experimental λ (Å)	RMBPT gA	Experimental intensities
		Ni-like Pd^{18+}				Ni-like Cd^{20+}			
$^3D_3$	$^3D_3$	264.927	264.832	13.4	12	234.179	234.043	16.6	15
$^3D_1$	$^3D_2$	265.997	266.435	8.41	5	235.322	235.536	10.9	7
$^3D_2$	$^3D_3$	268.927	269.247	7.23	9	237.532	237.859	9.48	8
$^3D_1$	$^3D_1$	269.941	271.523	17.3	8	239.999	240.074	21.6	5
$^1D_2$	$^3D_2$	270.298	270.183	12.0	9	238.725	238.514	14.9	7
$^3D_2$	$^1P_1$	271.542	271.523	10.7	8	240.307	240.258	15.9	4
$^3D_2$	$^3F_2$	274.197	274.645	16.0	17	242.350	242.817	20.5	15
$^3D_3$	$^3F_4$	277.674	277.985	18.3	20	245.325	245.222	23.1	20
$^1D_2$	$^1F_3$	277.727	277.610	18.0	17	244.859	244.850	23.0	10
$^3D_1$	$^3P_0$	284.250	287.837	18.1	3	253.611	253.677	22.0	7
$^3D_2$	$^3P_1$	289.793	289.330	6.93	3	256.412	256.410	6.84	3
$^3D_2$	$^1D_2$	293.548	293.810	1.82	2	260.870		1.76	
$^3D_1$	$^1P_1$	303.626	303.895	2.07	3	273.763		2.12	
$^1D_2$	$^1P_1$	309.244	308.776	4.50	3	278.380	277.851	4.02	5
$^3D_3$	$^3F_3$	326.636	326.804	4.09	8	296.753	296.622	4.86	8
$^3D_1$	$^1D_2$	331.406	332.095	5.67	10	300.773	301.276	6.57	7
$^3D_2$	$^3F_3$	332.738	333.550	6.57	8	302.159	302.800	7.54	12
$^1D_2$	$^3P_1$	333.137	332.010	6.37	5	300.225	299.640	8.50	10
$^3D_3$	$^3P_2$	335.292	334.356	9.96	15	303.965	302.975	11.3	15
$^1D_2$	$^1D_2$	338.109	337.928	3.44	10	306.355	306.315	4.34	7

is about 10% for many transitions. This difference can be explained by contribution of highly excited states that could not be taken into account by the RCN, RCG Cowan computer codes [50].

In table 5, wavelengths and electric-dipole transition rates are presented for 3d4s–3d4p transitions in Ni-like Pd^{18+} and Cd^{20+}. The RMBPT results are compared with experimental measurements by Churilov *et al* from [36]. We can see from table 5 that our wavelength results

Table 6. Wavelengths (λ in Å) and transition rates (gA in 10^{10} s^{-1}) for 3d4p–3d4d transitions in Ni-like ions. The RMBPT results are compared with experimental measurements by MacGowan *et al* in [37] ($Z = 63$ and 70), [38] ($Z = 73$ and 74), and [39] ($Z = 79$).

Ion	Experimental λ (Å)	RMBPT λ (Å)	RMBPT gA
	$3d_{5/2}4p_{3/2}$ (1)–$3d_{5/2}4d_{5/2}$ (1)		
$Z = 79$		65.54	24.0
$Z = 74$	75.35 ± 0.015	75.30	19.1
$Z = 73$	77.47 ± 0.02	77.47	18.2
$Z = 70$	84.40 ± 0.05	84.47	15.8
$Z = 63$	104.56 ± 0.05	104.57	11.2
	$3d_{5/2}4p_{3/2}$ (1)–$3d_{5/2}4d_{5/2}$ (2)		
$Z = 79$		63.02	11.5
$Z = 74$	72.40 ± 0.015	72.33	9.21
$Z = 73$	74.42 ± 0.02	74.40	8.81
$Z = 70$		81.09	7.70
$Z = 63$	100.39 ± 0.05	100.37	5.55
	$3d_{5/2}4p_{3/2}$ (1)–$3d_{3/2}4d_{3/2}$ (0)		
$Z = 79$		42.24	41.2
$Z = 74$		49.46	37.7
$Z = 73$	50.97 ± 0.02	51.07	37.0
$Z = 70$	56.09 ± 0.05	56.26	34.8
$Z = 63$	71.00 ± 0.03	71.10	29.4
	$3d_{3/2}4p_{1/2}$ (1)–$3d_{3/2}4d_{3/2}$ (0)		
$Z = 79$	35.605 ± 0.02	35.71	132.0
$Z = 74$	43.185 ± 0.01	43.231	81.9
$Z = 73$	44.83 ± 0.02	44.91	74.1
$Z = 70$	50.26 ± 0.05	50.35	55.0
$Z = 63$	65.83 ± 0.03	65.98	26.8

are in excellent agreement (0.04–0.2%) with experimental measurements. Our weighted transition rates for 3d4s–3d4p transitions are compared with intensities in relative units given in [36]. In most cases the gA values are proportional to the relative intensities; however, there are disagreements by a factor of 3–4 in some cases ($^3D_1$–$^3P_0$ and $^1D_2$–$^1D_2$ transitions). It should be noted that our RMBPT gA values slowly increase from Pd^{18+} to Cd^{20+}; however, the relative intensities increase in some cases ($^3D_3$–$^3D_3$ transition) and decrease in others ($^1D_2$–$^1F_3$ transition).

In table 6, wavelengths (λ in Å) and transition rates (gA in 10^{10} s^{-1}) are shown for the four 3d4p–3d4d transitions in Ni-like ions. The RMBPT results are compared with experimental measurements by MacGowan *et al* from [37, 38]. Experimental measurements for Ni-like Eu^{35+} and Yb^{42+} ions were reported in [37], however, the wavelength data for Ta^{45+} and W^{46+} are from [38]. Our values of wavelengths for the $3d_{5/2}4p_{3/2}$ (1)–$3d_{5/2}4d_{5/2}$ (1) and $3d_{5/2}4p_{3/2}$ (1)–$3d_{5/2}4d_{5/2}$ (2) transitions are in a good agreement within the experimental uncertainty of the measurements in [37, 38], however, there is less agreement for the wavelengths of the $3d_{5/2}4p_{3/2}$ (1)–$3d_{3/2}4d_{3/2}$ (0) and $3d_{3/2}4p_{1/2}$ (1)–$3d_{3/2}4d_{3/2}$ (0) transitions (the difference is a factor of 2–4 of the experimental uncertainty). We did not find any data in

Table 7. Lifetime values (τ in 10^{-9} s) of levels of Ni-like ions.

Level	$Z = 36$	$Z = 37$	$Z = 38$	$Z = 39$	$Z = 40$	$Z = 41$	$Z = 42$	$Z = 44$	$Z = 46$	$Z = 47$	$Z = 48$	$Z = 50$	Level-jj
$3d4d\,{}^1S_0$	2.72[−2]	2.03[−2]	1.64[−2]	1.37[−2]	1.16[−2]	1.01[−2]	8.75[−3]	6.80[−3]	5.67[−3]	5.16[−3]	4.66[−3]	3.96[−3]	$3d_{3/2}4d_{3/2}(0)$
$3d4d\,{}^3P_0$	4.11[−2]	3.70[−2]	3.14[−2]	2.72[−2]	2.39[−2]	2.11[−2]	1.90[−2]	1.54[−2]	1.30[−2]	1.19[−2]	1.10[−2]	9.55[−3]	$3d_{5/2}4d_{5/2}(0)$
$3d4d\,{}^1P_1$	4.95[−2]	4.14[−2]	3.52[−2]	3.08[−2]	2.71[−2]	2.42[−2]	2.18[−2]	1.79[−2]	1.55[−2]	1.43[−2]	1.33[−2]	1.17[−2]	$3d_{5/2}4d_{5/2}(1)$
$3d4d\,{}^3S_1$	4.75[−2]	4.07[−2]	3.49[−2]	3.04[−2]	2.69[−2]	2.38[−2]	2.13[−2]	1.74[−2]	1.46[−2]	1.33[−2]	1.21[−2]	1.03[−2]	$3d_{5/2}4d_{3/2}(1)$
$3d4d\,{}^3P_1$	4.36[−2]	4.05[−2]	3.45[−2]	2.99[−2]	2.63[−2]	2.33[−2]	2.09[−2]	1.69[−2]	1.41[−2]	1.27[−2]	1.18[−2]	9.83[−3]	$3d_{3/2}4d_{3/2}(1)$
$3d4d\,{}^3D_1$	4.28[−2]	3.90[−2]	3.31[−2]	2.86[−2]	2.53[−2]	2.24[−2]	2.02[−2]	1.66[−2]	1.43[−2]	1.31[−2]	1.22[−2]	1.08[−2]	$3d_{3/2}4d_{5/2}(1)$
$3d4d\,{}^1D_2$	4.28[−2]	3.63[−2]	3.06[−2]	2.64[−2]	2.30[−2]	2.02[−2]	1.80[−2]	1.45[−2]	1.49[−2]	1.38[−2]	1.28[−2]	1.12[−2]	$3d_{3/2}4d_{5/2}(2)$
$3d4d\,{}^3P_2$	4.39[−2]	3.66[−2]	3.12[−2]	2.69[−2]	2.36[−2]	2.09[−2]	1.86[−2]	1.51[−2]	1.25[−2]	1.13[−2]	1.04[−2]	8.81[−3]	$3d_{5/2}4d_{3/2}(2)$
$3d4d\,{}^3D_2$	4.60[−2]	3.86[−2]	3.28[−2]	2.87[−2]	2.52[−2]	2.25[−2]	2.02[−2]	1.66[−2]	1.42[−2]	1.31[−2]	1.23[−2]	1.07[−2]	$3d_{5/2}4d_{5/2}(2)$
$3d4d\,{}^3F_2$	4.52[−2]	3.98[−2]	3.40[−2]	2.97[−2]	2.61[−2]	2.33[−2]	2.10[−2]	1.73[−2]	1.19[−2]	1.09[−2]	9.95[−3]	8.36[−3]	$3d_{3/2}4d_{3/2}(2)$
$3d4d\,{}^1F_3$	4.62[−2]	3.81[−2]	3.24[−2]	2.79[−2]	2.44[−2]	2.14[−2]	1.90[−2]	1.53[−2]	1.25[−2]	1.13[−2]	1.04[−2]	8.68[−3]	$3d_{5/2}4d_{3/2}(3)$
$3d4d\,{}^3D_3$	4.74[−2]	3.78[−2]	3.20[−2]	2.76[−2]	2.41[−2]	2.13[−2]	1.90[−2]	1.52[−2]	1.26[−2]	1.15[−2]	1.05[−2]	8.86[−3]	$3d_{3/2}4d_{3/2}(3)$
$3d4d\,{}^3F_3$	4.71[−2]	3.97[−2]	3.40[−2]	2.95[−2]	2.61[−2]	2.32[−2]	2.09[−2]	1.74[−2]	1.47[−2]	1.37[−2]	1.27[−2]	1.11[−2]	$3d_{3/2}4d_{5/2}(3)$
$3d4d\,{}^3G_3$	4.68[−2]	3.90[−2]	3.32[−2]	2.90[−2]	2.56[−2]	2.29[−2]	2.06[−2]	1.71[−2]	1.47[−2]	1.36[−2]	1.27[−2]	1.12[−2]	$3d_{5/2}4d_{5/2}(3)$
$3d4d\,{}^1G_4$	5.11[−2]	4.09[−2]	3.51[−2]	3.06[−2]	2.71[−2]	2.42[−2]	2.18[−2]	1.82[−2]	1.54[−2]	1.43[−2]	1.34[−2]	1.17[−2]	$3d_{3/2}4d_{5/2}(4)$
$3d4d\,{}^3F_4$	4.80[−2]	4.01[−2]	3.43[−2]	2.98[−2]	2.63[−2]	2.34[−2]	2.11[−2]	1.74[−2]	1.48[−2]	1.37[−2]	1.27[−2]	1.11[−2]	$3d_{5/2}4d_{5/2}(4)$
$3d4d\,{}^3G_4$	4.57[−2]	3.84[−2]	3.25[−2]	2.79[−2]	2.45[−2]	2.16[−2]	1.92[−2]	1.55[−2]	1.28[−2]	1.16[−2]	1.06[−2]	8.93[−3]	$3d_{5/2}4d_{3/2}(4)$
$3d4d\,{}^3G_5$	4.91[−2]	4.15[−2]	3.56[−2]	3.11[−2]	2.75[−2]	2.46[−2]	2.22[−2]	1.84[−2]	1.57[−2]	1.45[−2]	1.35[−2]	1.18[−2]	$3d_{5/2}4d_{5/2}(5)$
Level	$Z = 54$	$Z = 56$	$Z = 63$	$Z = 70$	$Z = 73$	$Z = 74$	$Z = 76$	$Z = 79$	$Z = 82$	$Z = 83$	$Z = 90$	$Z = 92$	Level-jj
$3d4d\,{}^1S_0$	2.96[−3]	2.61[−3]	1.65[−3]	1.05[−3]	8.54[−4]	7.97[−4]	6.92[−4]	5.57[−4]	4.43[−4]	4.11[−4]	2.33[−4]	1.97[−4]	$3d_{3/2}4d_{3/2}(0)$
$3d4d\,{}^3P_0$	7.24[−3]	6.39[−3]	4.14[−3]	2.75[−3]	2.32[−3]	2.19[−3]	1.96[−3]	1.66[−3]	1.41[−3]	1.34[−3]	9.28[−4]	8.36[−4]	$3d_{5/2}4d_{5/2}(0)$
$3d4d\,{}^1P_1$	9.29[−3]	8.36[−3]	6.00[−3]	4.37[−3]	3.82[−3]	3.65[−3]	3.33[−3]	2.90[−3]	2.51[−3]	2.40[−3]	1.70[−3]	1.54[−3]	$3d_{5/2}4d_{5/2}(1)$
$3d4d\,{}^3S_1$	7.35[−3]	6.24[−3]	3.53[−3]	1.98[−3]	1.54[−3]	1.42[−3]	1.20[−3]	9.24[−4]	7.11[−4]	6.51[−4]	3.51[−4]	2.95[−4]	$3d_{5/2}4d_{3/2}(1)$
$3d4d\,{}^3P_1$	7.02[−3]	5.97[−3]	3.37[−3]	1.89[−3]	1.47[−3]	1.34[−3]	1.13[−3]	8.68[−4]	6.63[−4]	6.07[−4]	3.26[−4]	2.31[−4]	$3d_{3/2}4d_{3/2}(1)$
$3d4d\,{}^3D_1$	8.66[−3]	7.83[−3]	5.58[−3]	4.06[−3]	3.52[−3]	3.35[−3]	3.05[−3]	2.65[−3]	2.27[−3]	2.15[−3]	2.32[−4]	2.35[−4]	$3d_{3/2}4d_{5/2}(1)$
$3d4d\,{}^1D_2$	8.87[−3]	7.95[−3]	5.57[−3]	4.00[−3]	3.47[−3]	3.31[−3]	3.02[−3]	2.62[−3]	2.27[−3]	2.15[−3]	2.40[−4]	2.25[−4]	$3d_{3/2}4d_{5/2}(2)$
$3d4d\,{}^3P_2$	6.34[−3]	5.40[−3]	3.12[−3]	1.78[−3]	1.39[−3]	1.27[−3]	1.08[−3]	8.32[−4]	6.40[−4]	5.86[−4]	3.12[−4]	2.60[−4]	$3d_{5/2}4d_{3/2}(2)$
$3d4d\,{}^3D_2$	8.45[−3]	7.58[−3]	5.34[−3]	3.85[−3]	3.35[−3]	3.20[−3]	2.92[−3]	2.54[−3]	2.21[−3]	2.11[−3]	1.51[−3]	1.37[−3]	$3d_{5/2}4d_{5/2}(2)$
$3d4d\,{}^3F_2$	6.03[−3]	5.16[−3]	2.98[−3]	1.70[−3]	1.33[−3]	1.22[−3]	1.03[−3]	7.97[−4]	6.14[−4]	5.63[−4]	3.30[−4]	2.57[−4]	$3d_{3/2}4d_{3/2}(2)$
$3d4d\,{}^1F_3$	6.39[−3]	5.47[−3]	3.14[−3]	1.78[−3]	1.39[−3]	1.27[−3]	1.07[−3]	8.26[−4]	6.32[−4]	5.78[−4]	3.02[−4]	2.50[−4]	$3d_{3/2}4d_{3/2}(3)$
$3d4d\,{}^3D_3$	6.21[−3]	5.28[−3]	3.03[−3]	1.71[−3]	1.33[−3]	1.23[−3]	1.03[−3]	7.97[−4]	6.11[−4]	5.59[−4]	2.94[−4]	2.43[−4]	$3d_{5/2}4d_{3/2}(3)$
$3d4d\,{}^3F_3$	8.75[−3]	7.84[−3]	5.50[−3]	3.95[−3]	3.43[−3]	3.28[−3]	2.99[−3]	2.60[−3]	2.26[−3]	2.16[−3]	1.54[−3]	1.40[−3]	$3d_{3/2}4d_{5/2}(3)$
$3d4d\,{}^3G_3$	8.88[−3]	7.97[−3]	5.62[−3]	4.04[−3]	3.52[−3]	3.36[−3]	3.06[−3]	2.66[−3]	2.31[−3]	2.20[−3]	1.57[−3]	1.43[−3]	$3d_{5/2}4d_{5/2}(3)$
$3d4d\,{}^1G_4$	9.19[−3]	8.24[−3]	5.77[−3]	4.12[−3]	3.58[−3]	3.42[−3]	3.11[−3]	2.70[−3]	2.34[−3]	2.24[−3]	1.60[−3]	1.45[−3]	$3d_{3/2}4d_{5/2}(4)$
$3d4d\,{}^3F_4$	8.74[−3]	7.81[−3]	5.48[−3]	3.92[−3]	3.41[−3]	3.26[−3]	2.97[−3]	2.58[−3]	2.24[−3]	2.14[−3]	1.53[−3]	1.39[−3]	$3d_{5/2}4d_{5/2}(4)$
$3d4d\,{}^3G_4$	6.45[−3]	5.48[−3]	3.17[−3]	1.79[−3]	1.39[−3]	1.28[−3]	1.08[−3]	8.31[−4]	6.36[−4]	5.81[−4]	3.04[−4]	2.52[−4]	$3d_{5/2}4d_{3/2}(4)$
$3d4d\,{}^3G_5$	9.34[−3]	8.33[−3]	5.83[−3]	4.17[−3]	3.62[−3]	3.46[−3]	3.15[−3]	2.73[−3]	2.37[−3]	2.26[−3]	1.61[−3]	1.46[−3]	$3d_{5/2}4d_{5/2}(5)$

[37, 38] to compare our RMBPT values of weighted transition rates given in the last column of table 6.

3.3. Lifetime data

In table 7, we present a limited set (18 among 105) of our RMBPT lifetime data for the 3d4d LSJ levels in Ni-like ions with $Z = 36$–92. To avoid level identification problems, we present the LS and jj labels of the transitions and include both wavelengths and transition rates in table 7. We can see from this table that for ions with $Z = 36$–50 there are rather small differences (about 10–20%) in lifetimes of the individual levels, except the $3d4d\,{}^1S_0$ level. The difference increases for high-Z ions. For example, the ratio of largest and smallest lifetime values given in table 7 is equal to 1.9, 3.2 and 7.8 for ions with $Z = 36$, 54 and 92, respectively.

Results of the present calculation of the lifetimes are obtained by taking into account E1 transition rates from each upper level to all possible lower levels. The contributions of the different channels to the lifetimes of the $3d4d\,{}^{1,3}L_J$ levels with $J = 0$–3 are shown in figures 6 and 7. The curves represent the ratios of individual transition probabilities A to the

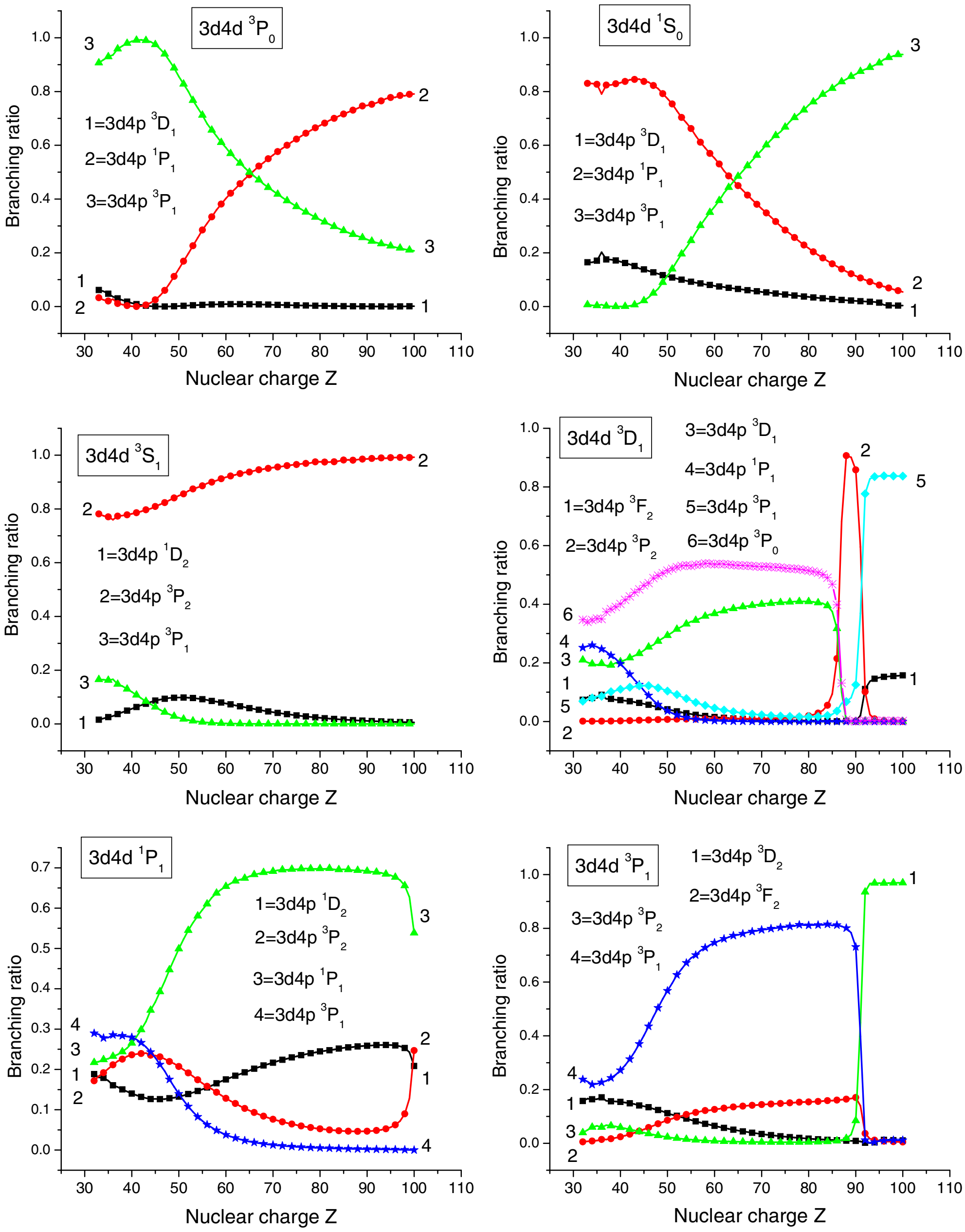

Figure 6. Channel contributions to the lifetimes of the 3d4d $^{1,3}L_J$ ($J = 0, 1$) states.

sum of all transition probabilities $\sum A$ for the level considered. As we see from the two upper panels of figure 6, the largest contribution to the lifetimes of the 3d4d ^{3}P$_1$ level comes from the 3d4p ^{3}P$_1$ state for low-Z ions and from 3d4p ^{1}P$_1$ state for high-Z ions. We have the opposite situation for the 3d4d $^1S_0$ level; the 3d4p ^{1}P$_1$ state gives the largest contribution for low-Z ions and the 3d4p ^{3}P$_1$ state gives the largest contribution for high-Z ions.

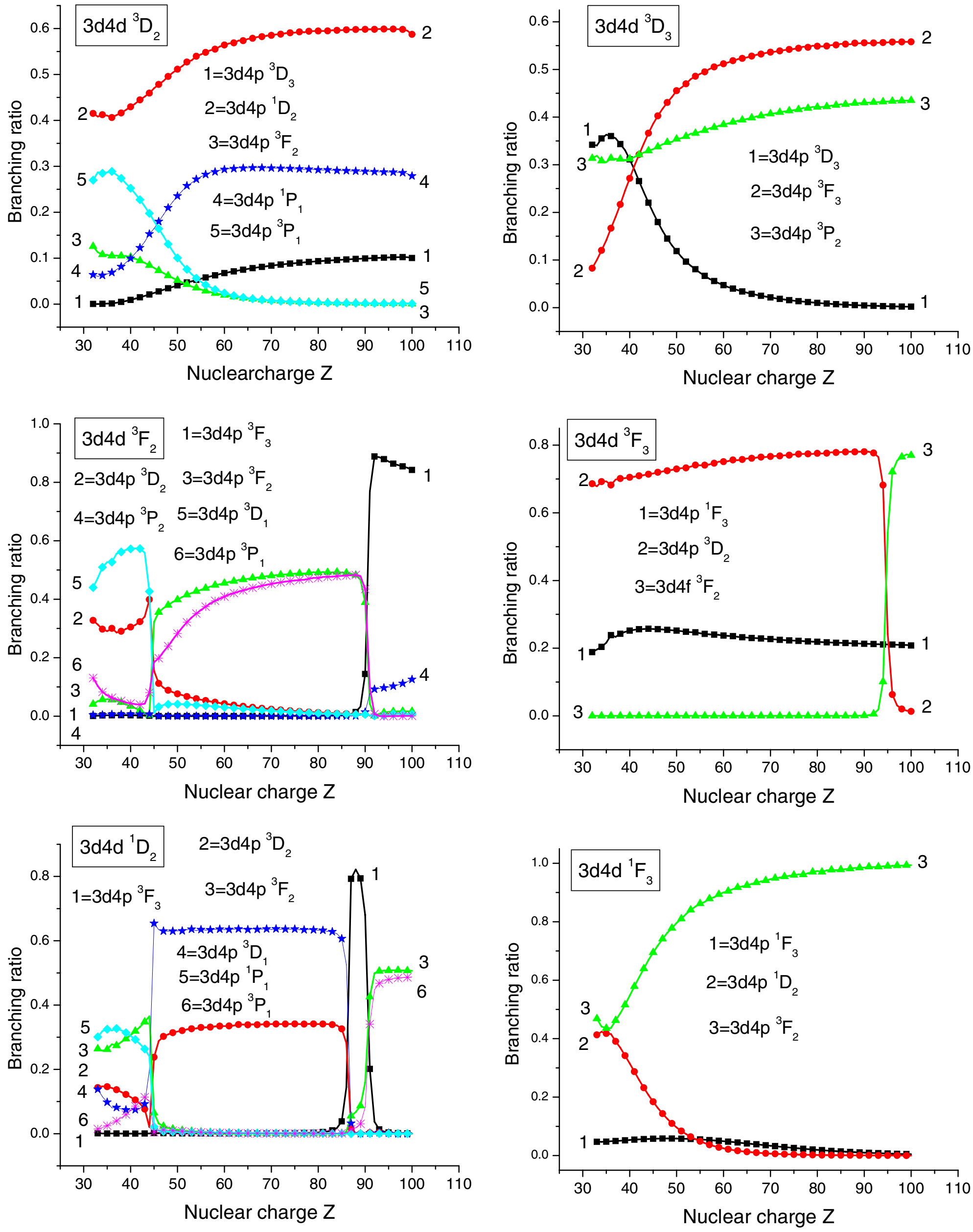

Figure 7. Channel contributions to the lifetimes of the 3d4d $^{1,3}L_J$ ($J = 2, 3$) states.

Only for two levels presented in figures 6 and 7, the dominant transition does not change for the entire range of Z; the 3d4p ^{3}P$_2$ − 3d4d ^{3}S$_1$ transition (the centre left panel of figure 6) and the 3d4p ^{1}D$_2$–3d4d ^{3}D$_2$ transition (the upper left panel of figure 7). The contribution of the dominant transition is 80–90% in the first case (the 3d4d ^{3}S$_1$ level); however, the contribution of the dominant transition for the 3d4d ^{3}D$_2$ level is only 40–60%.

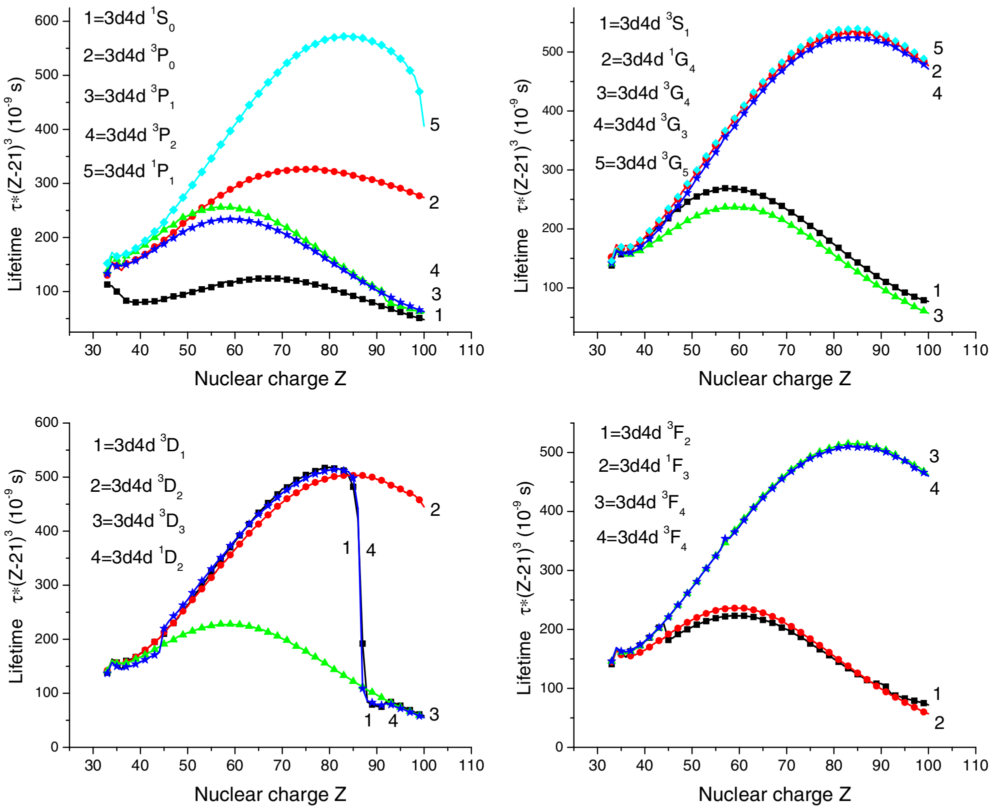

Figure 8. Lifetimes ($\tau \times (Z-21)^3$) of the 3d4d $^{1,3}L_J$ levels as function of Z in 10^{-9} s.

For low-Z ions it is difficult to determine the dominant transition. Three transitions (3d4p ^{3}P$_0$–3d4d ^{3}D$_1$, 3d4p ^{1}P$_1$–3d4d ^{3}D$_1$ and 3d4p ^{3}D$_1$–3d4d ^{3}D$_1$) have almost equal contribution (20–40%) to the lifetime of the 3d4d ^{3}D$_1$ level shown in the centre right panel of figure 6). A similar behaviour of the branching ratios for the lifetimes of the 3d4d ^{1,3}P$_1$ levels is seen on the two bottom panels of figure 6. Two transitions (3d4p ^{3}D$_3$–3d4d ^{3}D$_3$ and 3d4p^{3}P$_2$–3d4d ^{3}D$_3$) give the dominant and almost equal (30–35%) contributions to the lifetime of the 3d4d ^{3}D$_3$ level for the low-Z ions with $Z = 32$–40 (see the upper right panel of figure 7). We find the same behaviour of the branching ratios for the lifetimes of the 3d4d ^{3}F$_2$, 3d4d ^{1}D$_2$ and 3d4d ^{1}F$_3$ levels presented on the centre left and two bottom panels of figure 7.

An abrupt change of the dominant transition for very high-Z ions with $Z = 88$–92 occurs for the 3d4d ^{3}D$_1$, 3d4d ^{3}P$_1$, 3d4d ^{3}F$_2$, 3d4d ^{3}F$_3$ and 3d4d ^{1}D$_2$ levels, as illustrated by the centre left and bottom left panels of figure 6 and the two centre and bottom left panels of figure 7, respectively. Those abrupt changes in the branching ratio are caused by the dramatic change in Z-dependences of the transition rates (see figures 4 and 5). We already discussed previously that singularities in the transition-rate curves could be explained by one of three origins: avoided level crossings, zeros in the dipole matrix elements and zeros in transition energies. For example, the abrupt change in the branching ratio of the 3d4d ^{3}P$_1$ level (see the bottom left panels of figure 6) with nuclear charge $Z = 93$ is caused by the avoided level crossing of the 3d4d ^{3}P$_1$ and 3d4p ^{3}D$_2$ levels. There are three largest mixing coefficients $C^Q(3d_{3/2}4d_{3/2}(1))$, $C^Q(3d_{3/2}4d_{5/2}(1))$ and $C^Q(3p_{3/2}4p_{1/2}(1))$ when $Q = $ 3d4d ^{3}P$_1$ (see graph

4 in [3]). The value of the $C^Q(3d_{3/2}4d_{3/2}(1))$ coefficient dramatically decreases for $Z \geqslant 93$; however, the value of the $C^Q(3p_{3/2}4p_{1/2}(1)$ coefficient becomes equal to 1.0 for $Z \geqslant 93$. For high-Z ions, there is only one largest mixing coefficient $C^{Q'}(3d_{3/2}4p_{1/2}(1))$ when $Q' = 3d4p\,^3P_1$, however, there are two largest mixing coefficient $C^{Q'}(3d_{3/2}4p_{3/2}(2))$ and $C^{Q'}(3p_{3/2}4s_{1/2}(2))$ when $Q' = 3d4p\,^3D_2$ [3]. The values of these coefficients are inverted when $Z = 93$. Because of this change in mixing coefficients the branching ratio of the $3d4p\,^3D_2$–$3d4d\,^3P_1$ transition becomes dominant for $Z \geqslant 93$, instead of the $3d4p\,^3P_1$–$3d4d\,^3P_1$ transition. A similar explanation is found for the other four $3d4d\,^3D_1$, $3d4d\,^3F_2$, $3d4d\,^3F_3$ and $3d4d\,^1D_2$ levels. All those contributions are taken into account in the calculations of the lifetime data.

The general trends of the Z-dependences of the lifetimes multiplied by $(Z-21)^2$ for the $3d4d\,^{1,3}L_J$ levels in Ni-like ions are presented in figure 8. It should be noted that Z was decreased by 21 to provide better presentation of the lifetime data. The Z-dependences of lifetimes are smoother than the Z-dependence of the transition rates presented in figures 4 and 5. A sharp change in the trends of the lifetimes occurs in high-Z ions for the $3d4d\,^3D_1$ and $3d4d\,^1D_2$ levels shown on the bottom left panel of figure 8. We already mentioned that the branching ratios for the $3d4d\,^3D_1$, $3d4d\,^3P_1$, $3d4d\,^3F_2$, $3d4d\,^3F_3$ and $3d4d\,^1D_2$ levels change abruptly for high-Z ions. Abrupt changes for the $3d4d\,^3D_1$ and $3d4d\,^1D_2$ levels happen twice, at $Z = 87$ and 91, as shown on the central right panel of figure 4 and the bottom left panel of figure 5. Transition rates of those new transitions become larger for $Z \geqslant 87$ that leads to decreasing of lifetimes for the $3d4d\,^3D_1$ and $3d4d\,^1D_2$ levels shown in figure 8.

4. Conclusion

We have presented a systematic second-order relativistic MBPT study of the reduced matrix elements, oscillator strengths and transition rates for the $4s-4p$, $4p-4d$, $4d-4f$, $3s-3p$ and $3p-3d$ electric-dipole transitions in nickelike ions with the nuclear charge Z ranging from 34 to 100. Our retarded $E1$ matrix elements include correlation corrections from Coulomb and Breit interactions. Both length and velocity forms of the matrix elements were evaluated, and small differences, caused by the non-locality of the starting DF potential, were found between the two forms. Contributions from negative energy states were also included in order to improve the agreement between results calculated in lengths and velocity gauges. Second-order RMBPT transition energies were used in our evaluation of the oscillator strengths and transition rates. These calculations are compared with other calculations and with available experimental data. For $Z \geqslant 36$, we believe that the present theoretical data are more accurate than other theoretical or experimental data for transitions between $n = 4$ states in Ni-like ions. We hope that these results will be useful in analysing older experiments and planning new ones.

Acknowledgments

This research was sponsored by the National Nuclear Security Administration under Cooperative agreement 52-06NA27588. Work at LLNL was performed under auspices of the DOE under contract no W-7405-Eng-48.

References

[1] Safronova U I, Johnson W R and Albritton J R 2000 *Phys. Rev.* A **62** 052505
[2] Hamasha S M, Shlyaptseva A S and Safronova U I 2004 *Can. J. Phys.* **82** 331

[3] Safronova U, Safronova A S, Hamasha S M and Beiersdorfer P 2006 *At. Data Nucl. Data Tables* **92** 47
[4] Safronova U, Safronova A S, Hamasha S M and Beiersdorfer P 2006 *J. Phys. B: At. Mol. Opt. Phys.* **39** 4491
[5] Smith R F, Dunn J, Filevich J, Moon S, Nilsen J, Keenan R, Shlyaptsev V N, Rocca J J, Hunter J R and Marconi M C 2005 *Phys. Rev.* E **72** 36404
[6] Keenan R, Dunn J, Patel P K, Price D F, Smith R F and Shlyaptsev V N 2005 *Phys. Rev. Lett.* **94** 103901
[7] Kawachi T, Sasaki A, Tanaka M, Kishimoto M, Hasegava N, Nagashimo K, Koike F, Daido H and Kato Y 2004 *Phys. Rev.* A **69** 33805
[8] Janulewicz K A, Lucianetti A, Priebe G, Sandner W and Nickles P V 2003 *Phys. Rev.* A **68** 51802
[9] Mocek T *et al* 2003 *Proc. SPIE* **5197** 119
[10] Norreys P A *et al* 1993 *J. Phys. B: At. Mol. Opt. Phys.* **26** 3693
[11] Scofield J H and MacGowa B J 1992 *Phys. Scr.* **46** 361
[12] Chen M H and Osterheld A L 1995 *Phys. Rev.* A **52** 3790
[13] Li Y, Nilsen J, Dunn J, Osterheld A L, Ryabtsev A and Churilov S 1998 *Phys. Rev.* A **58** R2668
[14] Daido H, Ninomiya S, Takagi M, Kato Y and Koike F 1999 *J. Opt. Soc. Am.* B **16** 296
[15] Nilsen J, Dunn J, Osterheld A L and Li Y 1999 *Phys. Rev.* A **60** R2677
[16] King R, Aggarwal G J P K M, Keenman F P and Rose S J 2004 *J. Phys. B: At. Mol. Opt. Phys.* **37** 225
[17] Beiersdorfer P, Nilsen J, Osterheld A, Vogel D, Wong K, Marrs R and Zasadzinski R 1992 *Phys. Rev.* A **46** R25
[18] Elliott S R, Beiersdorfer P and Nilsen J 1995 *Phys. Rev.* A **51** 1683
[19] Elliott S R, Beiersdorfer P, MacGowan B J and Nilsen J 1995 *Phys. Rev.* A **52** 2689
[20] May M J, Fournier K B, Beiersdorfer P, Chen H and Wong K L 2003 *Phys. Rev.* E **68** 36402
[21] Shlyaptseva A *et al* 2004 *Rev. Sci. Instrum.* B **75** 3750
[22] Neill P, Harris C, Safronova A S, Hamasha S M, Hansen S, Safronova U and Beiersdorfer P 2004 *Can. J. Phys.* **82** 931
[23] Doron R, Fraenkel M, Mandelbaum P, Zigler A and Schwob J J 1998 *Phys. Scr.* **58** 19
[24] Zigler A, Mandelbaum P, Schwob J J and Mitnik D 1994 *Phys. Scr.* **50** 61
[25] Doron R, Fraenkel E B M, Mandelbaum P, Schwob J J, Zigler A, Faenov A Y and Pikuz T A 2000 *Phys. Rev.* A **62** 52508
[26] von Goeler S *et al* 1988 *J. Phys. (Paris) Colloq. C1* **49** 349
[27] Neu R, Fournier K B, Schlögl D and Rice J 1997 *J. Phys. B: At. Mol. Opt. Phys.* **30** 5057
[28] Fournier K B 1998 *At. Data Nucl. Data Tables* **68** 1
[29] Klapisch M, Schwob J J, Fraenkel M and Oreg J 1977 *J. Opt. Soc. Am.* **61** 148
[30] Zhang H L, Sampson D H and Fonts C J 1991 *At. Data Nucl. Data Tables* **48** 91
[31] Elliott S, Beiersdorfer P and Nilsen J 1994 *Phys. Scr.* **49** 556
[32] Skobelev Y, Dyakin V M, Faenov A Y, Bartnik A and Fiedorowicz H 1999 *J. Phys. B: At. Mol. Opt. Phys.* **32** 113
[33] Dong C Z, Fritzsche S and Xie L Y 2003 *J. Quant. Spectrosc. Radiat. Transfer* **76** 447
[34] Zhong J Y, Zhang J, Zeng J L, Zhao G and Gu M F 2005 *At. Data Nucl. Data Tables* **89** 101
[35] Wyart J-F and Ryabtsev A N 1986 *Phys. Scr.* **33** 215
[36] Churilov S S, Ryabtsev A N and Wyart J-F 1988 *Phys. Scr.* **38** 326
[37] MacGowan B J, Maxon S, Hagelstein P L, Keane C J, London R A, Matthews D L, Rosen M D, Scofield J H and Whelan D A 1987 *Phys. Rev. Lett.* **59** 2157
[38] MacGowan B J, Maxon S, Da Silva L B, Fields D J, Keane C J, Matthews D L, Osterheld A L, Scofield J H, Shimkaveg G and Stone G F 1990 *Phys. Rev. Lett.* **65** 420
[39] MacGowan B J *et al* 1990 *Proc. 2nd Int. Coll.* p 221
[40] Rahman A, Hammarsten E C, Sakadzic S, Rocca J J and Wyart J-F 2003 *Phys. Scr.* **67** 414
[41] Rahman A, Rocca J J and Wyart J-F 2004 *Phys. Scr.* **70** 21
[42] Churilov S S, Ryabtsev A N and Wyart J-F 2005 *Phys. Scr.* **71** 457
[43] Träbert E, Beiersdorfer P, Fournier K B, Utter S B and Wong K L 2001 *Can. J. Phys.* **79** 153
[44] Utter S B, Beiersdorfer P and Träbert E 2002 *Can. J. Phys.* **80** 1503
[45] Safronova U I, Johnson W R, Safronova M S and Derevianko A 1999 *Phys. Scr.* **59** 286
[46] Safronova U I, Derevianko A, Safronova M S and Johnson W R 1999 *J. Phys. B: At. Mol. Opt. Phys.* **32** 3527
[47] Safronova U I, Cowan T E and Safronova M S 2005 *J. Phys. B: At. Mol. Opt. Phys.* **38** 2741
[48] Chen M H, Cheng K T and Johnson W R 1993 *Phys. Rev.* A **47** 3692
[49] Ralchenko Yu, Jou F-C, Kelleher D E, Kramida A E, Musgrove A, Reader J, Wiese W L and Olsen K 2005 *NIST Atomic Spectra Database* (version 3.0.2), online. Available: http://physics.nist.gov/asd3 (4 January 2006) (Gaithersburg, MD: National Institute of Standards and Technology)
[50] URL http://das101.isan.troitsk.ru/cowan.htm
[51] Johnson W R, Blundell S A and Sapirstein J 1988 *Phys. Rev.* A **37** 307